

Nano-resolved sensing of 3D electromagnetic fields via single emitters' extreme variation of enhanced spontaneous emission

R. Margoth Córdoba-Castro,^{1, 2 *} Dirk Jonker,^{3, 4 †} Clement Cabriel,^{1 †} Mario Zapata-Herrera,⁵ Bart van Dam,¹ Yannick De Wilde,¹ Robert W. Boyd,^{2, 6} Arturo Susarrey-Arce,^{3, 4} Ignacio Izeddin^{1 *} and Valentina Krachmalnicoff^{1 *}

¹ Institut Langevin, ESPCI Paris, Université PSL, CNRS, 75005 Paris, France.

² Department of Physics, University of Ottawa, Ottawa, ON, Canada.

³ Department of Chemical Engineering, MESA+ Institute, University of Twente, P. O. Box 217, Enschede 7500AE, The Netherlands

⁴ Mesoscale Chemical Systems, MESA+ Institute, University of Twente, Enschede 7500AE, The Netherlands.

⁵ Donostia International Physics Center (DIPC), Paseo Manuel de Lardizabal 4, 20018 San Sebastian, Spain

⁶ University of Rochester, Institute of Optics, Rochester, NY, USA.

†These authors contributed equally.

*Corresponding authors. rcordova@uottawa.ca, ignacio.izeddin@espci.fr, valentina.krachmalnicoff@espci.fr.

Abstract

Controlling quantum light-matter interactions at scales smaller than the diffraction limit at the single quantum emitter level is a critical challenge to the goal of advancing quantum technologies. We introduce a novel material platform that enables precise engineering of spontaneous emission changes in molecular single emitters through 3D nanofields. This platform is based on a 3D hollow plasmonic nanomaterial arranged in a square lattice, uniformly scalable to the centimeter scale while maintaining unit cell geometry. This coupled system leads to billions of Purcell-enhanced single emitters integrated into a nanodevice. Using far-field single-molecule super-resolution microscopy, we investigate emission modifications at the single-emitter level, enabling molecular position sensing with resolution surpassing the diffraction limit. By combining the nanolocalization with time correlation single photon counting (TCSPC), we probe molecule per molecule enhanced quantum light-matter interactions. Despite the dense distribution of emitters across the 3D hollow geometry, our technique generates a nanometer-scale map of the Purcell factor for individual molecules. This 3D plasmonic geometry significantly enhances light-matter interactions, revealing a broad range of lifetimes—from nanoseconds to picoseconds—significantly increasing the local density of states (LDOS) in a manner that depends on both molecular position and dipole orientation, offering extreme position sensitivity within the 3D electromagnetic landscape. By leveraging these plasmonic nanostructures and our method for measuring single-molecule Purcell-enhanced nano-resolved maps, we enable fine-tuned control of light-matter interactions. This approach enables the on-demand control of fast single-photon sources at room temperature, providing a powerful tool for molecular sensing and quantum applications at the single-emitter level.

Keywords: single-molecule 3D sensing, spontaneous emission enhanced, far-field super-resolution microscopy, single-emitters, Purcell factor, LDOS enhancement, 3D hollow plasmonics.

Light serves as an ideal information carrier in both classical and quantum systems, as well as a powerful tool for probing matter. This has driven significant advancements in controlling light emission, absorption, and propagation through the development of specifically designed materials^{1,2,3}. Single photons, or quanta of light, are particularly advantageous due to their ability to travel long distances with minimal loss and decoherence^{4,5}. As such, single-photon sources are critical for emerging quantum technologies, including secure communications^{6,7}, quantum computing⁸, and ultra-sensitive quantum sensing of electromagnetic fields^{9,10,11}.

Purcell proposed using microcavities to modify the single-photon emission rate¹², Drexhage's pioneer work, experimentally showed that the emission rate of a two-level system is not an intrinsic property of a quantum system but depends on the environment¹³. The spontaneous emission rate of a single emitter increases with the availability of photonic states to radiate into, defined as the local density of states (LDOS) or its dimensionless counterpart (i.e. normalized to the LDOS in vacuum), often called the Purcell factor^{12,13,14,15,16,17,18}. Reliable control of spontaneous emission involves engineering the electromagnetic environment to tune decay rates, emission locations, and emitter's directions^{14,15,16,17,18,19}.

Studying spontaneous emission at the single-photon level and observed with a resolution surpassing the diffraction limit provides deep insights into an emitter's surroundings, enabling the development of highly sensitive and scalable sensing platforms that are potentially deployable in large light emitting networks embedded in a single device^{9,10,11,12}. Nanostructured media, particularly metal-based nanophotonic materials supporting localized surface plasmon resonances (LSPR), offer significant control over the electromagnetic environment^{20,21,22}, enhancing photonic states and accelerating quantum transitions to create bright, fast quantum light sources¹⁶⁻³⁴.

Molecular quantum emitters are uniquely advantageous due to their small size, well-defined transition dipole moments, and tunable emission spectra²⁸. These properties make them ideal for applications such as nanoscopic sensing of pressure, strain, temperature, and electromagnetic fields^{9,10}. Their ease of fabrication, scalability, and compatibility with hybrid devices further position them as competitive single-photon sources and nonlinear elements for integrated platforms^{35,36,37,38,39}.

However, integrating quantum emitters with nanostructured materials presents challenges, namely: i) Fabricating nano- and micro-architectures with high field confinement and enhancement. ii) Precisely positioning emitters in high-LDOS regions. iii) Interrogating single emitters without perturbing the system. iv) Isolating single-emitter signals from background or neighboring emissions. v) Determining the exact emission location within the nanostructure. Overcoming these challenges enables super-resolution

non-invasive quantum nanometrology, allowing the detection of minute electromagnetic field variations with unprecedented sensitivity^{40,19}.

In this work, we couple molecular single emitters to a novel 3D plasmonic material platform⁴¹ that supports rich optical modes and nanoscale hotspots with extreme field enhancement (>600x according to simulations). This platform is scalable to centimeter-sized samples while maintaining precise morphological control. Using far-field single-molecule fluorescence lifetime imaging microscopy (FLIM)^{40,42,43,44}, we stochastically activate and interrogate individual emitters⁴⁶, achieving nanometer-scale localization maps that reveal up to 100× enhancement in spontaneous emission decay rates at room temperature. The enhancement depends strongly on the emitter's position and dipole orientation, as well as the illumination angle.

This scalable, cost-effective platform, fabricated with wafer-scale precision, offers a robust foundation for next-generation quantum photonics and ultra-sensitive optical sensing, paving the way for transformative advances in quantum technologies.

3D electromagnetic landscapes along plasmonic truncated hollow nanocones: extreme field enhancement with highly dispersive modes

Nanostructured metals—whether single particles, arrays, or metamaterials such as antenna dimers, nanodisks, nanocubes, nanotriangles, nanocrosses, or bowtie nanoantennas—are widely employed to manipulate electromagnetic environments^{22,47,48,49,50,51}. They present tailorable optical modes with strong dependence on the boundary conditions that bring localized light in sub-wavelength features. The accessibility on modify widely the geometric parameters offer flexibility in engineering plasmonic modes and tuning the local density of photonic states across desired spectral ranges. Conversely, three-dimensional (3D) geometries exhibit richer electromagnetic resonances due to the additional degree of freedom of electron mobility in metals, supporting longitudinal modes at oblique illumination angles^{52,53,54}. While conventional fabrication techniques like electron beam lithography (EBL) are suitable for creating 2D nano- or microstructures, alternative methods must be developed for fabricating complex 3D nanomaterials^{41,52,53,55}. Self-assembly techniques have successfully produced nanorod-^{52,54} and nanocone-based⁵³ metamaterials, demonstrating capabilities for dispersive mode generation and high field enhancement^{52,53,54,55}. Among the various geometries for plasmonic light control, hollow nanostructures offer more confined electromagnetic fields, strong field enhancements, less dissipation losses and reduced quenching of localized surface plasmon resonances (LSPR) due to plasmon hybridization^{56,57}. These features make hollow geometries particularly promising for designing advanced plasmonic materials with superior properties compared to solid nanostructures. Thanks to their intense plasmonic fields, hollow metal nanostructures have applications in sensing, surface-enhanced Raman scattering (SERS), photothermal cancer therapy, drug delivery, and catalysis, often outperforming in their solid counterparts^{41,56,57}. However, challenges remain in scaling up the fabrication while maintaining uniformity and reproducibility across large areas, especially for wafer-scale production of extended chip architectures.

We propose coupling quantum emitters to a novel nanomaterial platform composed of hollow plasmonic truncated nanocones arranged in a square nanolattice. This platform can be fabricated at a centimeter scale (Fig. 1), maintaining consistent unit cell size and nanostructure orientation across the entire array. The nanostructures were created using a redeposition method that combines subtractive hybrid lithography (SHL) with Talbot lithography and I-line photolithography for precise nano- and macroscale patterning⁴¹. Additional details of the fabrication process are provided in the Methods section. Fig. 1a-c shows the geometry of these hollow gold truncated nanocones (HTC) and their compact dimensions. The bottom and top outer diameters are 140 nm and 90 nm, respectively, with an inner top diameter of 70 nm, resulting in a top ring thickness of approximately 10 nm. The nanostructures are 240 nm high and arranged periodically with a 250 nm pitch in a square lattice, as shown in Fig. 1a. The fabrication process allows for centimeter-scale production with wafer-scale precision and morphology control (Fig. 1d and S1).

The hollow structures exhibit a rich variety of modes due to their inherent asymmetric geometry along the longitudinal axis. To analyse the excitation of them in a wide spectral range, we first investigated their optical response under varying illumination angles, from normal incidence ($\theta = 0^\circ$) to oblique ($\theta = 40^\circ$), using p-polarized white light. The nanostructures display a highly dispersive behavior with multiple plasmonic modes within the visible spectrum. Fig. 1e shows the measured extinction spectra of HTC immersed in water, recorded as the incidence angle θ increases from 0° to 40° . At small angles, two prominent extinction peaks are observed around 525 nm and 660 nm, associated to bonding and antibonding modes. As the angle increases, a third peak appears near 780 nm at $\theta=20^\circ$, which becomes more pronounced at larger angles—indicating the excitation of a longitudinal mode. Notably, increasing the incident angle causes a slight blue shift of the longitudinal mode by several tens of nanometers, while the peak near 620 nm shifts marginally toward longer wavelengths. Additionally, the peak around 525 nm diminishes with increasing angle, and a new, prominent peak emerges near 700 nm at $\theta\approx 40^\circ$, further emphasizing the complex dispersive nature of these modes.

Full-wave simulations using the Finite Element Method (FEM) were performed to analyze the near-field distribution and enhancement under both normal and oblique incidence of p-polarized plane waves in an infinite square array of Au hollow truncated cones (Fig. 1f-i). The field enhancement maps were generated at wavelengths corresponding to the resonances observed in the calculated extinction spectra (Fig. S2). The simulations reveal that, at approximately 600 nm, the electromagnetic field is broadly distributed along the 3D structure, while at around 700 nm, the field is highly localized at the top of the truncated cone. Notably, under oblique illumination, the hotspot intensity is localized in the top ring reaches values of extreme field enhancement (>600).

This behavior is attributed to the conical geometry's efficiency in exciting the longitudinal localized surface plasmon resonance (LSPR), resulting in extreme field enhancement at the top of the nanostructure at higher incidence angles—unlike nanorod structures, where the longitudinal dipolar LSPR is primarily confined at the bases⁵³. The tilted walls (relative to the vertical axis) promote strong field confinement at the apex, while the hollow architecture further concentrates the electromagnetic field within a very small volume around the top ring.

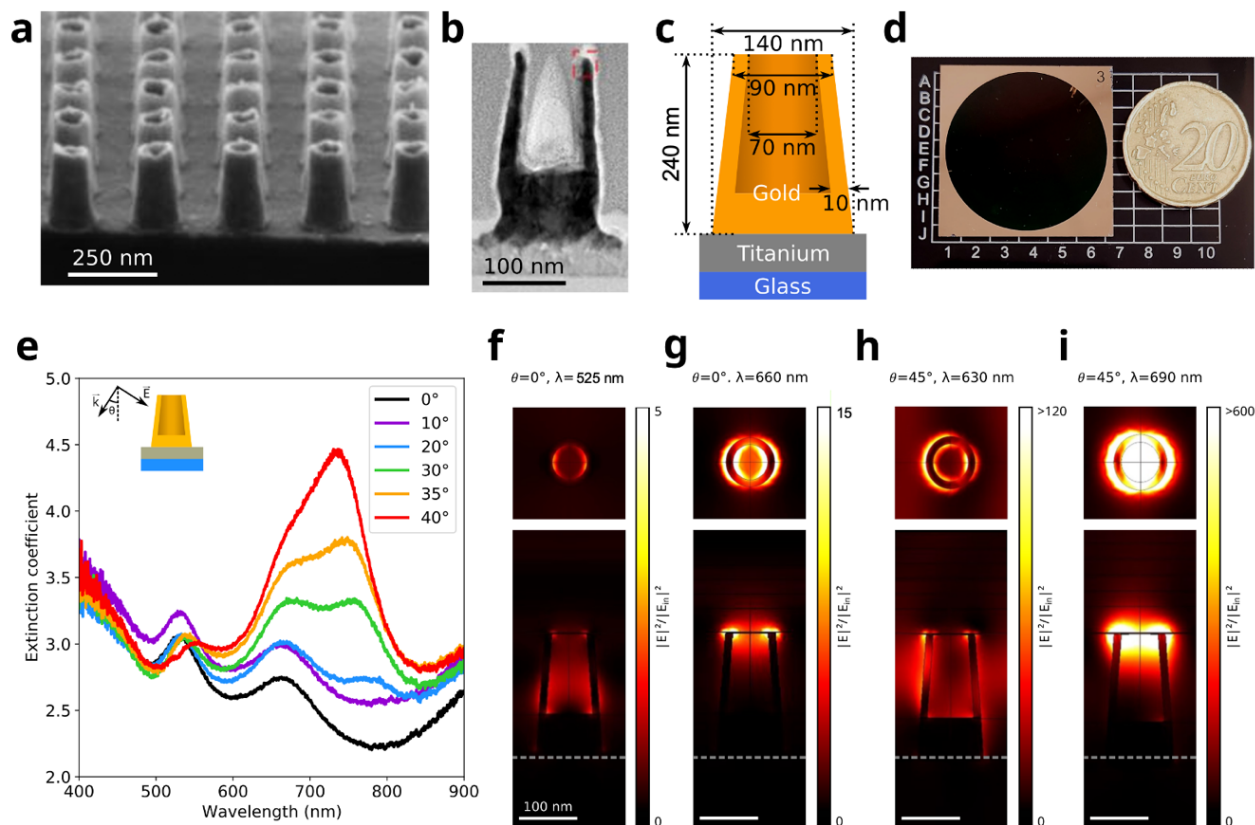


Figure 1: 3D Engineered electromagnetic environment (a-c) Images of the hollow gold truncated nanocone (HTC) fabricated on a square lattice with a period of 250 nm. (a) scanning electron microscopy (SEM) image showing the individual HCT and the array. (b) Transmission electron microscopy (TEM) section of a single structure. (c) Schematic summarizing the dimensions of the unit cell containing a single HTC. (d) The HTC square lattice can be fabricated uniformly in a centimeter scale chip, as shown on the photograph. (e-i) Optical characterization of the plasmonic resonances supported by the plasmonic nanostructure array. (e) Measured extinction spectra when the array is illuminated with *p*-polarized plane wave at different illumination angles θ with respect to the axis of the nanocones. (f,i) Calculated field enhancement maps for (f,g) normal and (h,i) oblique illuminations. Scale bars: 100 nm.

Simulations indicate that this field enhancement depends on the illumination conditions and can be tuned by increasing the excitation angle. Results for various wavelengths and angles are provided in [Supplementary Fig. S2](#). This 3D electromagnetic environment, combined with the incident field, will serve as the excitation basis for coupling single emitters to these advanced nanostructures, enabling the detection of fluorescence emission at the single-molecule level.

Super-resolved light-matter interaction enhancement at the single-molecule level

The fluorescence lifetime, $\tau = 1/\Gamma$, is a measurable quantity that allows straightforward experimental probing of the local density of optical states (LDOS) at the emitter's position^{14,15,16,17,18}. To investigate single emitters interacting with our 3D plasmonic structures, we coupled organic molecules to the hollow truncated cones and performed single-molecule fluorescence lifetime imaging (smFLIM), interrogating each molecule individually and localizing its position with nanoscale resolution.

Inspired by single-molecule localization microscopy (SMLM) techniques such as photoactivated localization microscopy (PALM) and stochastic optical reconstruction microscopy (STORM), smFLIM enables super-resolution localization of individual fluorescent molecules while simultaneously measuring their spontaneous emission lifetimes. To achieve this combined temporal and spatial resolution, we developed a custom-built single-molecule super-resolution microscope. This system correlates signals from an electron-multiplying CCD (EMCCD) camera with those from an array of eight single-photon avalanche diodes (SPADs) integrated with a time-correlated single-photon counting (TCSPC) system, providing picosecond temporal resolution^{40,42,43,44,45,46}.

The principle of the experiment is illustrated in Fig. 2a-b. The sample under study is labeled with photoactivatable fluorophores, and the illumination parameters of the photoactivation light source are optimized to reach the single-molecule regime. Unlike previous approaches where fluorophores are embedded in a polymer matrix—resulting in a random spatial distribution—our sample is chemically functionalized to produce a dense monolayer of fluorophores that bind specifically to the gold surface at a proximity of approximately 4 nm (see Methods). Upon pulsed laser excitation, photons emitted by each active molecule pass through a 50:50 beam splitter and are detected by two systems: an EMCCD camera, which determines the spatial position of each molecule, and a SPAD array, which measures the molecule's spontaneous emission lifetime. We conducted continuous acquisitions over several hours, capturing data with both the EMCCD (30 ms exposure) and the SPADs. The photoactivation power was carefully optimized to ensure two key conditions: 1) The point spread functions (PSFs) recorded on the EMCCD are sparse enough to be localized individually—that is, separated by more than the diffraction limit (~250 nm), with each PSF corresponding to a single emitter. 2) Each SPAD detects signals from at most one molecule at a time. This means that if two molecules within the 10- μm -wide area emit simultaneously, their PSFs must be separated by more than 1 μm —the center-to-center distance between the SPADs. If this separation isn't maintained, the data for both molecules are discarded.

This approach results in an emitter density below 1 molecule per μm^2 , which is critical for our technique to measure the emission properties of single emitters independently, avoiding simultaneous detection of neighboring molecules. We achieved this density by optimizing the photoactivation laser power and molecular deposition.

To determine the total spontaneous emission decay rate, Γ_t (the sum of radiative and non-radiative decay rates), of each single emitter, pulsed excitation was used in conjunction with time-correlated single-photon counting (TCSPC). This method records the fluorescence decay $S(t) = S \exp\left(\frac{-t}{\tau}\right)$ where $\tau = 1/\Gamma_t$ is the excited-state lifetime. The repetition rate of the pulsed laser was set to 39 MHz allowing sufficient relaxation of the emitter to the ground state before the arrival of the next pulse. Decay rates were obtained by fitting the decay curves with a single-exponential model.

The emission data from individual molecules, detected by both the camera and SPADs, was accumulated over several hours to achieve a high density of localized molecules (>5,000 molecules/ μm^2). This high density is essential for performing super-resolution imaging of the nanoscale lattice over an extended area. The coordinates and

fluorescence lifetimes of each detected molecule were then correlated to associate their spatial positions with their respective decay rates. Using this information, we reconstructed a super-resolved Purcell-enhanced map of single emitters with precise super-localization. Our smFLIM setup enables the measurement of lifetimes as short as a few tens of picoseconds and position precision of approximately 14 nm within a 10 μm^2 field of view^{40,44}. The customized TCSPC system combined with the SPAD array offers an excellent balance of high detection efficiency (>30% at 650 nm) and low timing jitter (<60 ps FWHM), ensuring reliable temporal and spatial resolution across the extended sample area. Detailed information on sample preparation, experimental setup, and data processing procedures can be found in the [Methods](#) section.

Reconstructed super-resolved images are shown in [Fig. 2c-e](#). These images reveal eight regions, each roughly 1 μm in diameter, corresponding to the conjugated areas in the camera's field of view associated with each SPAD in the array. The full detection density and intensity maps over a 10 μm^2 area, captured by the EMCCD camera, are presented in [Supplementary Fig. S3](#)). [Fig. 2c](#) displays the density map of detected molecules, with a median localization precision of approximately 14 nm. This high precision enables clear resolution of the 250-nm square lattice, with the measured sizes showing good agreement with the scanning electron microscopy images in [Fig. 2f](#). [Fig. 2d](#) presents the super-resolved map of total decay rate enhancement, normalized to the average value ($\Gamma_0 = 0.3 \text{ ns}^{-1}$) measured for the same fluorophores attached to a glass coverslip and immersed in water. Notably, there is significant variation in the decay rate enhancements, likely reflecting differences in emitter positioning relative to the nanopillars. [Fig. 2e](#) shows the super-resolved intensity map, derived from the integral of the Gaussian fit to each molecule's PSF. Similar to the decay rate map, there is a noticeable variation in intensity across the nanopillars. Interestingly, the emission remains largely unquenched despite the close proximity of the fluorophores to the metallic structures. These super-resolved maps highlight the complex and rich light-matter interactions occurring at these nanoscale dimensions.

Single-molecule supercell

To enhance the statistical robustness of our measurements, we leveraged the array's square periodicity and the symmetry of the nanostructures to merge the thousands of detected events into a single *supercell*. The steps involved in this data processing protocol are schematized in [Fig. 3a](#). First, the super-resolved maps shown in [Fig. 2](#) were post-processed to identify the center of each nanostructure and to establish a 2D square lattice used to merge all individual hollow truncated cones (HTCs) into one unified supercell. Although the period (250 nm) is known with high precision, the lattice orientation and origin had to be determined for each acquisition. This was achieved by overlaying SEM images onto the detected array, as shown in [Fig. S4](#), allowing us to accurately calculate the lattice angle. Using this information, the single-molecule localization data was divided into 250 \times 250 nm square unit cells, each centered on a single HTC. These unit cells were then recombined to form a single supercell, encompassing all detected molecules within the 8 SPADs array.

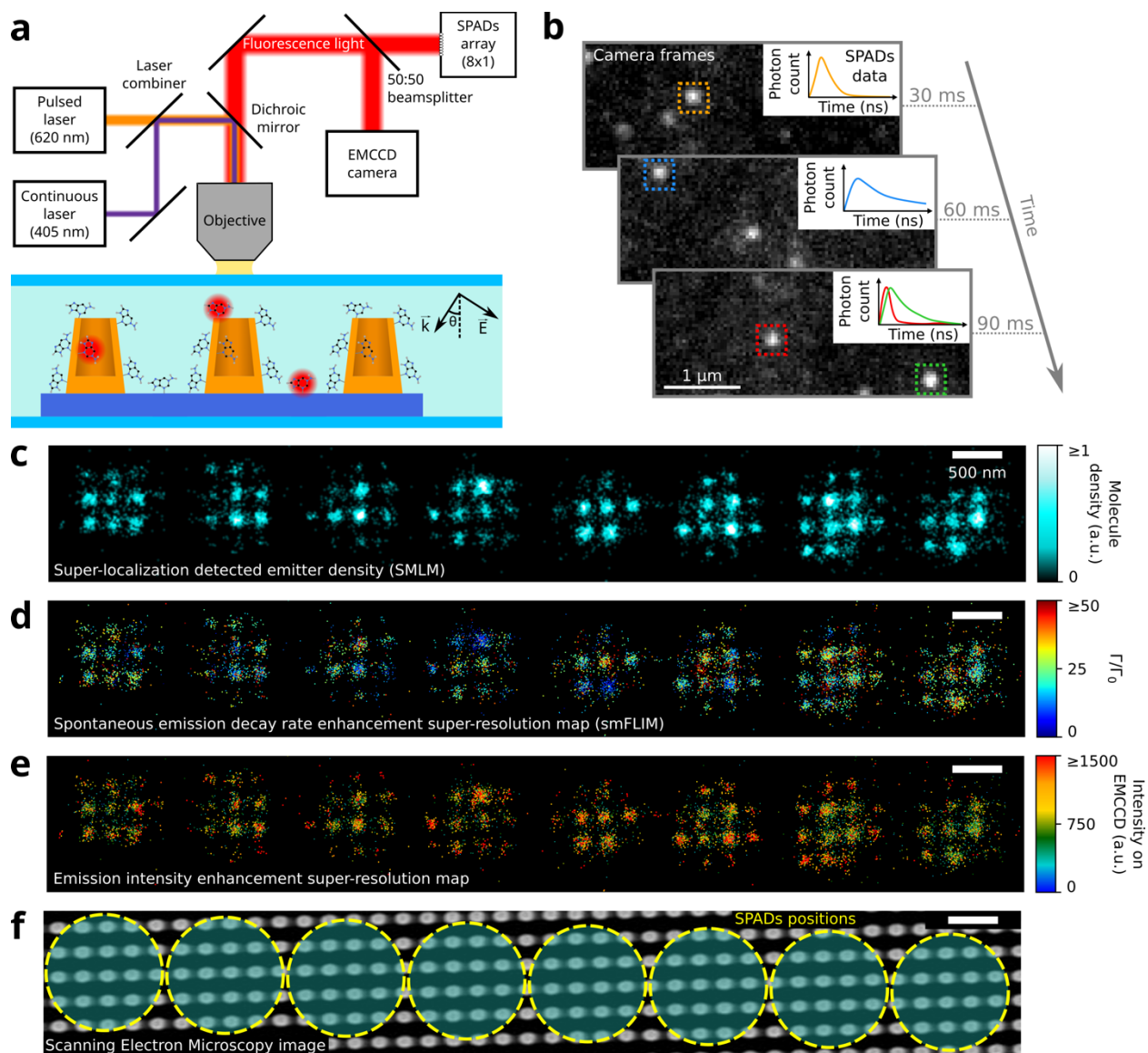


Figure 2: Nano-resolved light-matter interaction maps. a) Schematic showing the simplistic version of the optical setup and the sample mounting. b) Principle of the smFLIM experiment: on each EMCCD frame, the emitting molecules are detected (dotted color squares) and localized to measure their positions, which are correlated to the decay rate curves detected by the different SPADs (top right insets). This allows the molecule-per-molecule mapping of the Purcell enhancement of the single emitters with a resolution below diffraction limit. c-e) Super-resolved maps of single emitter detections in an area of $10 \mu\text{m}^2$ for an oblique *p*-polarized pulsed laser illumination at 620 nm. Various types of information are displayed: the detection density of molecules, represented as a pixelized map (c), and the total decay rate enhancement (d) and collected fluorescence intensity (e) maps for each molecule. The latter two are displayed as scatter plots where each point is a detected molecule, the color standing for the decay rate enhancement or the intensity. f) SEM image showing the corresponding field of view and the positions of the eight SPADs (yellow dashed circles). Scale bars: $1 \mu\text{m}$ (b), 500 nm (c-f).

Since each SPAD has a diameter of approximately 1 μm —and thus contains roughly 8 complete hollow nanopillars—the supercell contains approximately 64 times more molecules than a single pillar. This significantly improves the statistical power of the analysis (see Fig. S4 for more details).

The results obtained from this supercell approach are shown in Fig. 3b-g. The increased molecule count enabled a more detailed analysis of emitter decay rates and intensities, specifically in relation to their spatial positions within the supercell, particularly with respect to the center of each nanopillar.

Fig. 3c shows the decay rate enhancement measured within the supercell for molecules attached on the 3D nanostructure. As depicted in Fig. 3, higher decay rates are observed under oblique illumination compared to normal incidence, primarily due to increased field enhancement at the top ring and the excitation of longitudinal modes in the truncated conical shape. In some cases, the emission rate is accelerated by more than 50-fold. Interestingly, not only the decay rate but also the PSF intensity detected on the EMCCD—that is, the number of photons collected per molecule—is enhanced when the emitter interacts with the plasmonic system, as shown in Fig. 3d. Display of full datasets of molecule detections across the EMCCD and SPAD arrays within the large-area super-resolved map are provided in Fig. S5 for normal illumination.

To explore the influence of molecular position and orientation, we conducted an experiment where we prevented molecules from attaching to the inner surfaces of the nanopillar by filling the cavity with a polymer, as schematically illustrated in Fig. 3e. As expected, this reduced the overall density of detected molecules (Fig. 3f). As expected, the decay rate enhancement increases for oblique illumination similarly to the case without the polymer. However, the decay rate enhancement under oblique illumination increased similarly to the case without the polymer. Removing molecules from inside the hollow cone accentuates the effects of the tilted geometry; in this scenario, the decay rate map under oblique illumination shows more pronounced enhancement, especially near the center of the supercell. This behavior is also evident in the fluorescence intensity maps shown in Fig. 3g. Supplementary Fig. S6 provides SEM images confirming that the polymer coating is confined within the cavity throughout the large-area sample. The full-area maps of detected molecules for both normal and oblique illumination, with the cavity filled with polymer, are shown in Supplementary Fig. S7 and S8 respectively. Collectively, these observations suggest that the photophysical properties of the single molecules—particularly their quantum yield—are optimized at the center of the hollow structure. This enhancement results from the interaction of the emitters with localized plasmonic hotspots, which strongly influence emission rates and intensities²⁴⁻³¹.

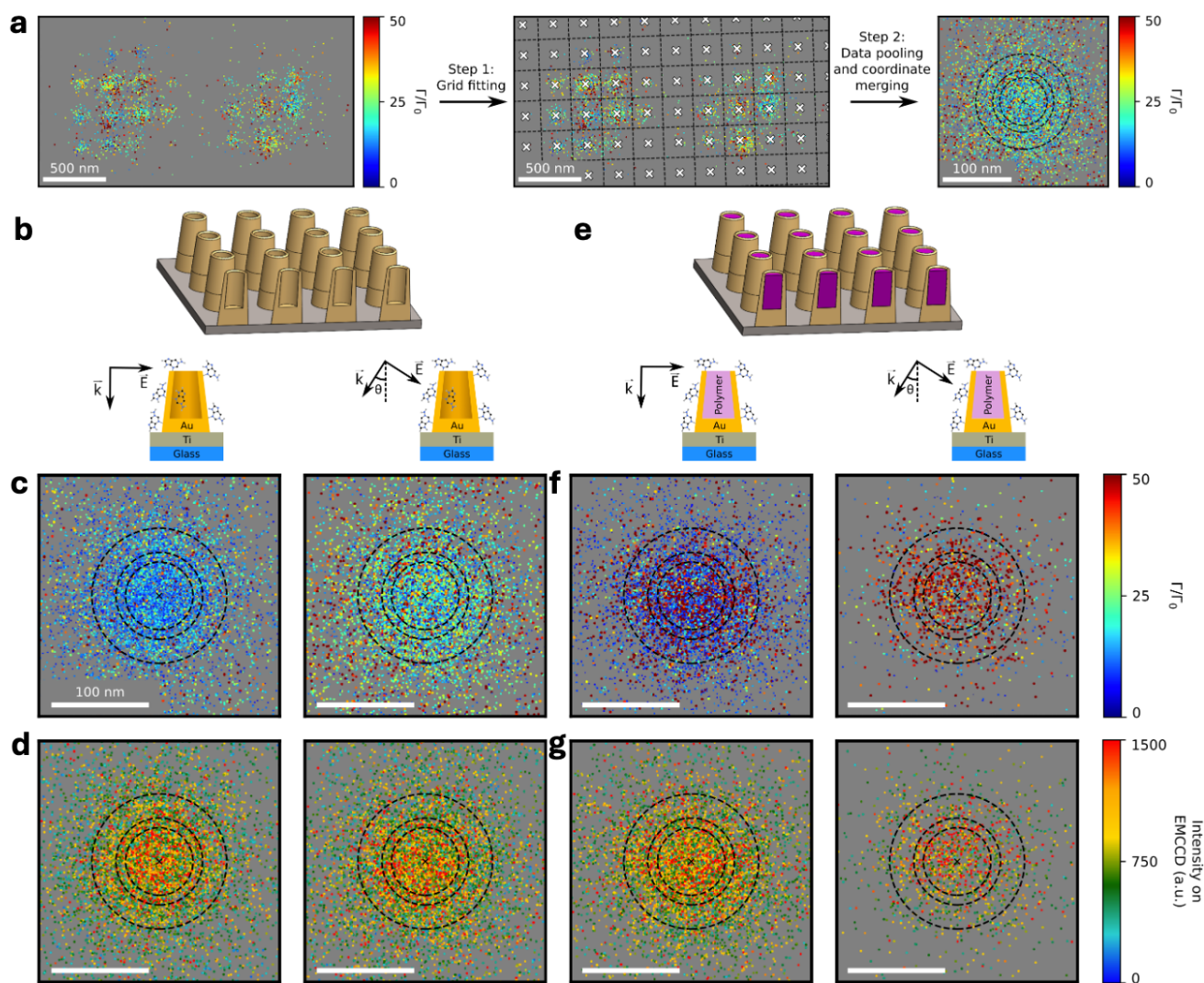


Figure 3: Spatial distribution of the measured decay rate enhancement on the supercell for empty and filled cavities, at normal and oblique illumination. (a) Representation of the post-processing steps to merge the acquired data in the $10\ \mu\text{m}^2$ field of view (for clarity reasons, only a region of $2.5\ \mu\text{m}$, i.e. two SPADs, is displayed here) to a $250\times 250\text{nm}$ unit cell. (b) Schematic illustrating the normal and oblique illumination conditions for a sample where the cavities are empty. (c) Total decay rate enhancement maps in the ‘supercell’, normalized to the average value obtained for molecules attached on a glass coverslip $\Gamma_0 = 0.3\ \text{ns}^{-1}$, for normal and oblique illuminations on a sample with empty cavities. (d) Intensity (i.e. number of photons detected on the EMCCD per 30-ms frame) maps in the ‘supercell’, for normal and oblique illuminations on a sample with empty cavities. The dotted circles stand for (from the outer to the inner one) the diameter of the base of the HTC, the outer diameter of the top ring and the inner diameter of the top ring (140 nm, 90 nm and 70 nm respectively), as defined in Fig. 1c. (e) Schematic illustrating the normal and oblique illumination conditions for a sample where the cavities are filled with polymer, preventing molecules from attaching inside the cavity. (f,g) Total decay rate enhancement (f) and intensity (g) maps in the ‘supercell’, for normal and oblique illuminations on a sample with polymer-filled cavities. All the maps

are displayed as scatter plots, with each molecule being represented as one point. Scale bars: 500 nm (a left and center), 100 nm (a right, c,d,f,g).

3D Variation of LDOS with emitter's position and excitation angle

To explore how the spontaneous emission decay rate depends on spatial position within the nanostructure, we examined the normalized decay rate, Γ/Γ_0 , as a function of the emitter's distance from the pillar's center. Our technique's strength lies in simultaneously recording the emission properties of individual emitters, enabling detailed correlations and analyses at the molecular scale. Fig. 4 a-d present a point cloud visualization of Γ/Γ_0 in the $(x, y, \Gamma/\Gamma_0)$ space, merging data from thousands of emitters within a supercell across four different experimental configurations. To better understand the spatial variation, Fig. 4 e-h depict the radial distribution of the same data, segmented into distinct decay enhancement intervals. The black dashed lines mark the radii corresponding to the inner top radius (35 nm), outer top radius (45 nm), and radius of base of the cone (70 nm).

We first focus on the unfilled structures, where emitters can attach anywhere on the gold surface, including inside the cavity. Under normal incidence (Fig. 4 a,e), the decay rate enhancement is mostly below 20. In contrast, under oblique illumination at approximately $\theta \approx 30^\circ$ (Fig. 4 b,f), the decay rate significantly increases, with many values exceeding the maximum temporal resolution of our setup ($\Gamma_{\text{Max}} = 50 \text{ ns}^{-1}$). Most molecules are localized near the supercell center, and the broad range of measured decay rates reflects the high sensitivity of the measurements to the emitter's precise position within the nanostructure.

As shown in Fig. 4g,h, filling the cavity with a polymer results in a pronounced decrease in the occurrence of decay enhancement values between 20 and 30. This reduction occurs because the polymer prevents molecules from binding inside the cavity, where moderate field enhancement occurs. Under normal illumination with the cavity filled, most decay enhancements are below $\Gamma/\Gamma_0 = 20$, with a small fraction exceeding $\Gamma/\Gamma_0 = 40$. In contrast, under oblique illumination, the fraction of emitters exhibiting strong decay rate enhancement increases dramatically (Fig. 4f,h). This aligns with the understanding that these high enhancement instances ($\Gamma/\Gamma_0 > 40$) originate from molecules located at the top of the hollow nanopillars. As demonstrated by the simulations in Fig. 1f-l, oblique illumination excites a longitudinal mode of the hollow truncated cone, resulting in intense field enhancement at the structure's apex.

Plotting the distribution of Γ/Γ_0 across the four configurations (Fig. 4i-l). further supports this interpretation. Specifically, adding polymer inside the cavity reduces the occurrence of decay enhancement values between 20 and 30 (comparing panels k,l to i,j), while tilting the illumination increases the occurrence of enhancements exceeding 40 (comparing panel l to k). These results confirm that lifetime measurements alone are sufficient for molecular sensing of the 3D electromagnetic field within or outside the nanostructure using these 3D hollow plasmonic systems.

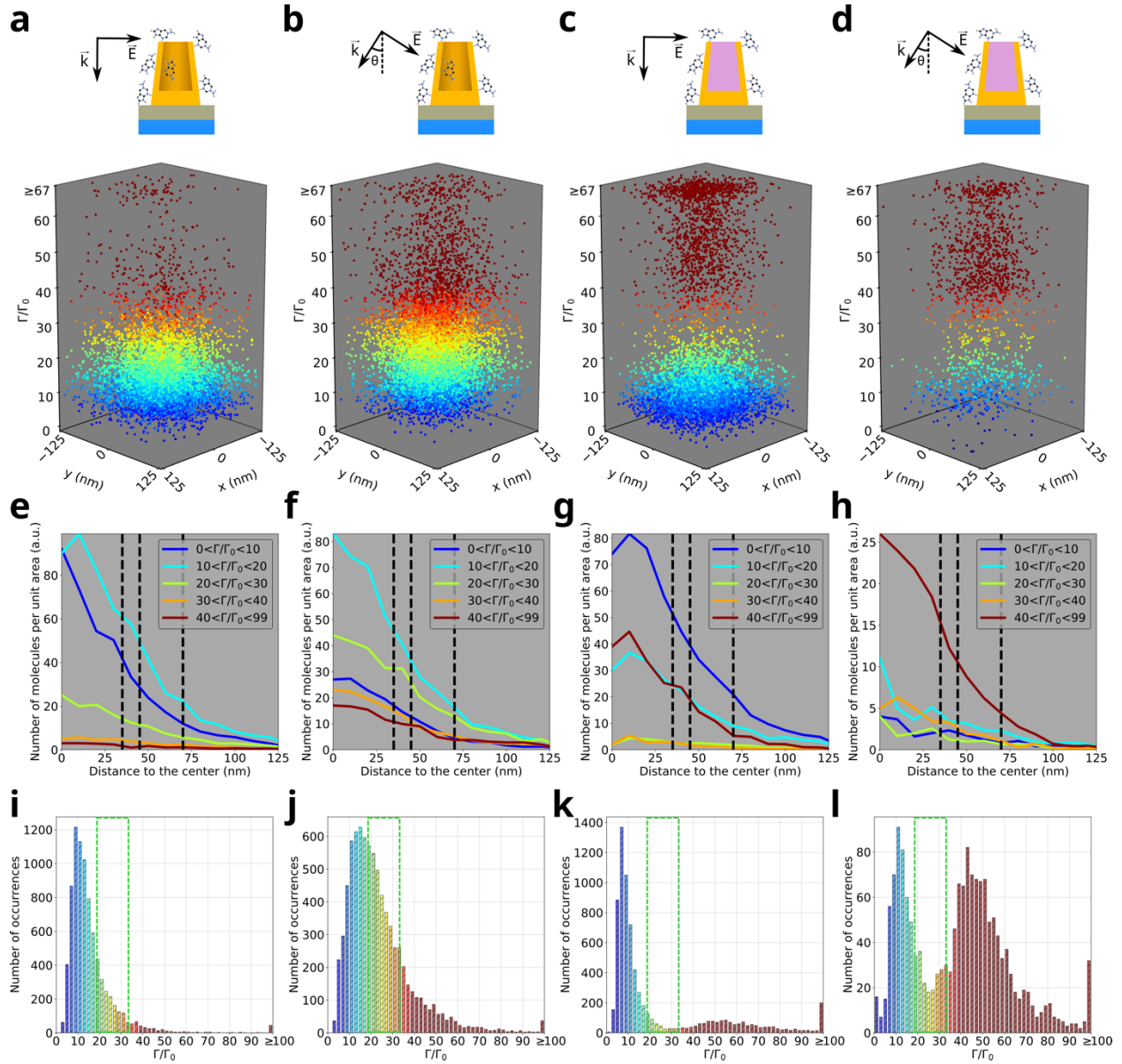


Figure 4: Position dependence of spontaneous emission rate enhancement a-d) Spatial distributions of the measured decay rate enhancement of all the data, plotted as a supercell for different experimental conditions. Each dot represents a molecule, and the color and height encode its measured decay rate. e-h) Radial distributions of the molecular density for different intervals of decay rate enhancement, plotted from the center to the edge of the supercell (125 nm). The black dashed lines stand for (from left to right), the inner radius of the top ring, the outer radius of the top ring and the radius of the base of the HTC (35 nm, 45 nm and 70 nm respectively), as defined in Fig. 1c. i-l) Histograms of the measured decay rate enhancement. The green dotted rectangles indicate the typical decay rate enhancement range for molecules inside the cavity, i.e. those that are blocked by the polymer. Throughout the figure, the results are presented for empty (a,b,e,f,i,j) and filled (c,d,g,h,k,l) cavities, and for normal (a,c,e,g,i,k) and oblique (b,d,f,h,j,l) illuminations.

A nanoantenna can amplify the emitted power of an excited two-level system with fixed energy $\hbar\omega$ in the weak coupling regime. As shown in Fig. 3, our 3D nanoantenna can significantly modify both the spontaneous emission rate and fluorescence intensity. Fluorescence intensity measurements reflect a combined enhancement of absorption and radiative emission, in addition to photons radiated by the nanoantenna. Conversely, lifetime data provide insight into the total spontaneous emission rate, including radiative Γ_r and nonradiative Γ_{nr} contributions. Our smFLIM approach enables disentangling these effects by simultaneously measuring decay rate enhancement and fluorescence intensity within the same system.

The spatial distribution of detected fluorescence intensity for molecules within the supercell is shown in Fig. 5a-d. Notably, emission is not quenched; a radiative contribution persists in all cases. The highest fluorescence intensities are observed for molecules near the center of the supercell, with broader, lower-intensity signals distributed toward the edges. The intensity point cloud visualization of the detected molecules exhibit a smooth increase from the edges toward the center, with the distribution sharply peaked at the supercell's center—demonstrating the remarkable super-localization precision of our method. This spatial pattern aligns with the conical geometry of the nanostructure and reflects the distance-dependent nature of both enhanced excitation and coupled emission. Importantly, the position where more efficiently enhanced emission is presented is at the supercell center and corresponds with the highest field enhancements predicted by the simulations in Fig. 1f-l, confirming the critical role of the nanostructure's geometry in dictating electromagnetic coupling at the single-molecule level.

Our measurements reveal a complex light-matter interaction involving both radiative and non-radiative channels. Fig. 5e-h illustrate this by showing the molecule-by-molecule correlation between the total decay rate and the detected fluorescence intensity.

Interestingly, a bimodal distribution appears only when the emitters are not within the cavity of the conical pillar (Fig. 5 g,h). This stochastic, far-field approach demonstrates the capacity to determine the excited-state lifetime and nanoscale-positioning of individual molecular quantum emitters, enabling molecule-specific characterization of both far-field and near-field light-matter interactions at super-resolution. Understanding these results, particularly those shown in Fig. 4 and 5, requires considering how the distribution of field enhancement varies with the excitation angle (Fig. 1f-i). At normal incidence, the excitation field predominantly enhances the region near the base of the nanostructure, leading to an under-representation of molecules located on the top ring—where the highest decay rate enhancements are expected. This is likely the primary reason why higher decay rate enhancements are observed under oblique illumination (Fig. 4j,l) compared to normal incidence (Fig. 4i,k), regardless of whether the cavities are filled with polymer.

The distribution of Γ/Γ_0 depends not only on the emitter's position relative to the nanopillars but also on the orientation of its dipole moment. To validate the experimental observations, we performed numerical simulations of the local density of optical states (LDOS) for various emitter positions and dipole orientations.

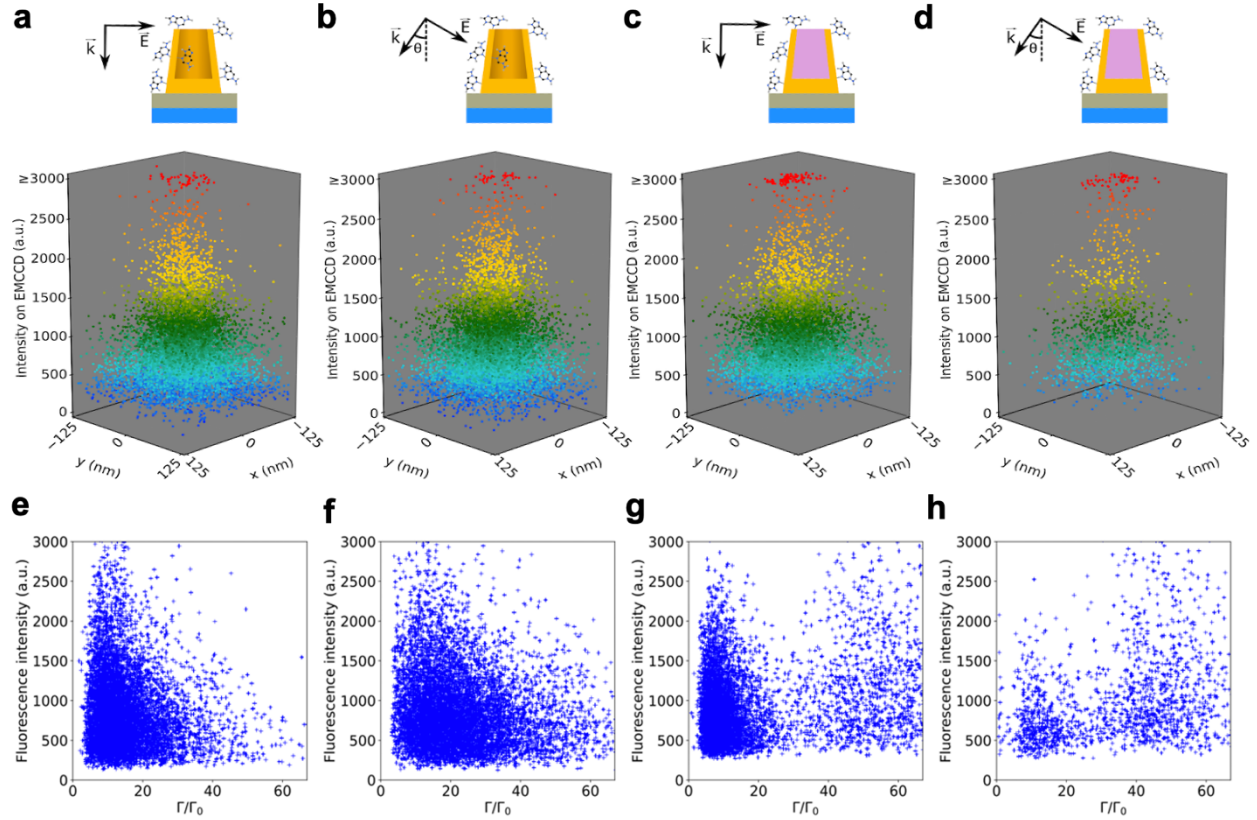


Figure 5. Measurement of the coupled emission fluorescence intensity, highlighting the radiative contribution of the enhanced molecule per molecule light-matter interaction for single emitters coupled to the 3D hollow conical pillar. a-d) Spatial distributions of the measured fluorescence intensity (defined as the number of photons detected in the PSF per EMCCD frame, i.e. per 30 ms) for each molecule, displayed as a supercell scatter plot, each dot representing one detected molecule. The color and height stand for the intensity. e-h) Molecule per molecule correlation of the fluorescence intensity with the decay rate enhancement, displayed as a scatter plot where each cross represents one detected molecule. The total decay rate is normalized with respect to the measured value of the emitter decay rate on glass surrounded by water ($\Gamma_0 = 0.3 \text{ ns}^{-1}$). Note that the positions of the molecules are not displayed in this representation. The data is presented without (a,b,e,f) and with the cavity filled (c,d,g,h) with a polymer, and for normal (a,c,e,g) and oblique (b,d,f,h) illuminations.

In the electric dipole approximation, appropriate for small quantum emitters at optical frequencies, the light-matter interaction is dominated by the dipolar response. Here, the Purcell factor effectively represents a change in the dielectric environment's impedance, linking the emitter's spontaneous decay rate to the impedance seen by a classical dipole antenna¹⁶. The radiative Γ_r and non-radiative Γ_{nr} decay rates can be derived within this framework. For a classical dipole, the total emitted power P can be partitioned into radiative and non-radiative components. The radiative power, P_R , corresponds to the energy emitted into the far-field, while the non-radiative power P_{NR} accounts for absorption within the nano-environment, including dark and guided modes in the near-field.

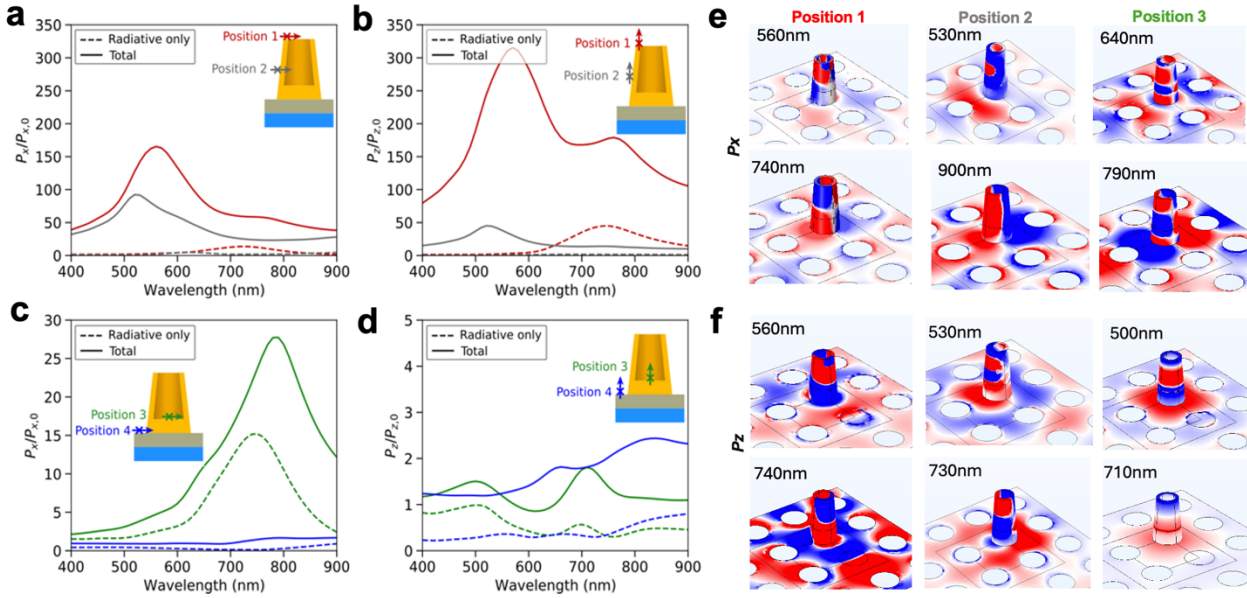


Figure 6: Calculated response of a point source coupled to the HTC. a-d) Simulated total and radiative decay rate enhancements for a dipole attached to the outer wall of the HTC (separated by 4 nm) at different positions and with different dipole orientations (see the insets). The decay rate calculated on the top ring (position 1) is higher than the one sensed by the dipole on the outer wall (position 2) or inside the cavity (position 3) for both dipole moment orientations. Note the different y axes in (a-d). e-f) Charge distribution for electric dipoles at different positions and with different electric dipole polarizations. Each disk represents one HTC.

The total enhanced decay rate $\Gamma_t = \Gamma_r + \Gamma_{nr}$ can be computed by integrating the near-field Poynting flux over a spherical surface with a radius of a few nanometers enclosing the emitter, effectively capturing both radiative and non-radiative contributions.

We numerically solved Maxwell's equations to analyze the interaction of single electric dipoles with the hollow truncated gold nanocone (HTC) at various positions \mathbf{r}_i , considering two distinct dipole orientations (in-plane and out-of-plane), across the visible spectrum. To assess the enhanced radiated power, we simulated finite square arrays of increasing size, monitoring the convergence of the results. Ultimately, a 10×10 lattice was used, which effectively approximates a semi-infinite array for a dipole positioned within the first four HTC unit cells at the center.

The local density of optical states (LDOS) modification was then quantified as the ratio of the power emitted by a dipole—placed 4 nm from the gold surface with a specific orientation—to the power emitted by an identical dipole located on a glass substrate in water. This ratio provides access to the total LDOS modification, incorporating both near-field and far-field contributions. The results of these simulations are shown in Fig. 6a-d, for various positions and dipole orientations P_x , P_z , as depicted in the insets.

The calculated total decay rate enhancement values vary depending on the emitter position: the highest values are observed for dipoles placed on the top ring of the truncated cone (position 1), relatively high for those on the outer walls (position 2), moderate for dipoles inside the cavity (position 3), and the lowest for dipoles near the base of the cone (position 4). When no emitters are present inside the hollow nanostructure—such as when the HTC cavity is filled with polymer (i.e., no molecules at position 3)—we expect the measured enhancement distribution to be bimodal, with low values (<10 at position 4) and high values (>20 at positions 1 and 2). This is consistent with our experimental data, where a clear bimodal distribution is visible in [Fig. 4k,l](#) when no molecules are inside the cavity.

Conversely, molecules inside the cavity are anticipated to exhibit intermediate decay rate enhancements, filling the gap between these high and low values. Such a bimodal distribution is not observed in [Fig. 4i,j](#). To verify this, we performed additional calculations for positions 1, 2, and 4 with the cavity filled with a polymer of refractive index 1.6 ([Fig. S9](#)). These show similar total and radiative decay rates compared to the data in [Fig. 5a-d](#), with only slight shifts toward longer wavelengths at the maximum values. The simulations reveal a dominance of the non-radiative component of the LDOS across all scenarios; however, in some cases, there is a significant enhancement of the radiative decay rate. For instance, at position 1 around 750 nm, the radiative contribution is nearly enhanced 50-fold ([Fig. 6b](#)).

The wide range of decay rate enhancement values observed in our measurements can be better understood by examining the charge distributions ([Fig. 6e,f](#)). For each position and dipole orientation, a variety of photonic modes are excited by the point source, leading to diverse electromagnetic responses. These calculated charge distributions vary across the spectral range, exhibiting dipolar, quadrupolar, octupolar, and more complex charge patterns depending on position and orientation. The conical geometry influences the emergence of different modes around both the top ring and the base, favoring the presence of dark modes within the visible spectrum. This is evident in [Fig. 6a and 6b](#) where the maximum total enhancement does not coincide with the peak of the radiative contribution.

Localized plasmonic modes near the top ring can be seen in the charge distributions for position 1 (top of the cone), as shown in [Fig. 6e and 6f](#), for both dipole orientations. For the dipole at position 2, an enhanced LDOS peak appears around 530 nm, characterized by a hexapolar-like charge distribution for both polarizations. At longer wavelengths, in-plane polarization exhibits a dipolar charge pattern, while along the longitudinal axis, a quadrupolar-like distribution appears near 730 nm. These are qualitatively examples of the possible modes supported by the structure. Additional simulations for dipole orientations along the y-axis are presented in [Supplementary Fig. S10](#), along with charge distributions at position 4, which display an even broader variety of modes. The pronounced position- and orientation-dependent behavior in this noncanonical conical geometry explains the significant variation observed in decay rate enhancements. Different modes are excited depending on the emitter's specific location and dipole orientation, resulting in diverse electromagnetic responses.

Single-molecule nanophotonics is an emerging field offering exciting opportunities to investigate light-matter interactions at the emitter level with nanometer-scale resolution. Our methodology, capable of temporally and spatially correlating enhanced single-emitter properties with super-resolved precision, heralds advances in technologies limited by resolution, single-photon efficiency, sensitive detection, low-density sensing, and vectorial field mapping. Integrating single-molecule detection with quantum sensors could significantly benefit chemical separation and analysis platforms. For instance, coupling quantum sensor sensitivity with microfluidics could pave the way for miniaturized devices capable of molecular-scale chemical separation and analysis^{58,59}.

Unlike many other quantum emitters, molecules exist as zero-dimensional entities with a fixed size below 5 nm. Their minimal steric hindrance allows them to access small features deep within complex samples, making them highly effective reporters for mapping electromagnetic landscapes in three dimensions. This contrasts with quantum dots, which generally have broader size and shape distributions—on the order of tens of nanometers—and are therefore less suited for dense sampling at the nanoscale.

Compared to smFLIM, other techniques do not allow to retrieve information about the density of states deep in the volume of the sample, most super-resolution approaches for light-matter interaction, such as scanning near-field optical microscopy (SNOM) rely on AFM tips for scanning surface topography, offering primarily superficial information. Our methodology opens an alternative window into understanding light-matter interactions in a minimally invasive manner—without perturbing the system with external metallic scanning probes^{18,19}.

The structure we studied comprises a large-scale array of 3D hollow truncated nanocones arranged in a square lattice, extending uniformly over centimeter scales while preserving the unit cell geometry for billions of identical nanostructures. This hollow plasmonic platform exhibits diverse and tunable light-matter interaction enhancement properties. The conical geometry renders the system highly sensitive to molecular nano-positioning—creating substantial spatial variations in the photonic density of states within the structure. These unique properties offer an exceptionally sensitive platform for molecular sensing and the detection of small vectorial field variations. Unlike solid nanostructures, hollow nanodevices provide an extended plasmonic surface area that enhances sensing capabilities and reduces energy losses. Their small feature sizes generate extreme electromagnetic field localization and intense enhancement. The tilted geometry supports a rich variety of photonic modes under polarized plane wave excitation, with the modes markedly dependent on the emitter's nano-position within the structure—an effect that becomes even more pronounced when the hollow is blocked, and emitters are coupled solely to the outer surface.

Conclusions:

In this work, we have introduced a novel platform and a methodology to precisely control and investigate spontaneous emission lifetimes at the nanoscale. This enables detailed observation of light-matter interactions beyond the diffraction limit, facilitating molecular

localization with nanometric precision, and allowing for single-molecule-level interrogation and ultra-precise nano-positioning analysis. Our approach reveals unprecedented, high non-averaged Purcell factors, demonstrating significant potential for quantum applications and sensing technologies.

We demonstrate that emission performance can be substantially improved through simultaneous enhancement of both radiative and non-radiative decay rates of individual molecular emitters. Crucially, this emission modification is highly dependent on the emitter's spatial position within the 3D hollow nanostructure and the illumination angle. The hollow plasmonic conical geometry offers a robust solution for mitigating plasmonic losses, while simultaneously supporting diverse 3D dispersive modes. This geometry introduces directionality and high LDOS sensitivity, enabling precise control over the emission properties based on the molecule's position and dipole orientation.

By analyzing thousands of single-molecule emission lifetimes with high sensitivity and dynamic range, we gain deep insights into the interactions between quantum emitters and complex nanostructured environments. The extreme variations in decay rates and emission intensities, mapped in relation to molecular position, provide valuable understanding of nanoscale light-matter coupling and enable detection of subtle electromagnetic field changes—both at the surface and deep within the 3D near-field landscape. These super-resolved measurements allow us to simultaneously map molecular positions and their modified spontaneous emission rates, directly linking quantum light-matter interactions to the local photonic environment.

Our findings demonstrate that this platform can enhance emitter quantum yields and achieve picosecond-scale spontaneous emission lifetimes at room temperature. Furthermore, it is produced as a wafer-scale device, with reproducible emission-rate enhancements patterned at the nanoscale across centimeter-sized areas. This scalability underscores the platform's remarkable potential as a reproducible, high-precision quantum sensing solution for future nanoscale photonic and quantum technologies.

Methods:

Hollow Conical Pillars Fabrication.

The fabrication of hollow Au nanopillars utilizes subtractive hybrid lithography (SHL), combining displacement Talbot lithography (DTL) which is utilized to generate a self-image by exposing a periodic phase-shift mask with a monochromatic light source.

The large area nanofabrication approach for precise nano- and macroscale patterning is presented in ⁴¹. The DTL/SHL is proven useful as it benefits from the best aspects of the two lithography techniques, e.g., resolution, rapidness, patternability, cost-effectiveness, and a single mask layer. First, a resist pattern is generated on a substrate, enabling high-resolution control over the nanoscale dimensions of the structures. Our method employs a single photoresist and two exposure techniques to generate a nanopatterned photoresist and bottom anti-reflective coating (BARC) to form a nanopillar-like structures at particular substrate locations. Subsequently, gold is deposited onto the patterned resist through the sputter-redeposition process, forming dense arrays of hollow nanopillars arranged in a square lattice with a 250 nm pitch. The nanopillars act as a template for the

sidewall redeposition of Au during angled ion beam etching (IBE). An angled etching step during IBE controls the redeposition rate, different from IBE performed at normal incidence reported in other studies.

The fabricated Au hollow nanopillars feature a solid base with a thickness of 90 ± 2 nm and a diameter of 140 ± 4 nm, while the nano-rims are 240 ± 10 nm high with a 12 ± 3 nm sidewall rim thickness. The BARC remains in the hollow of the structure after the sputtered-redeposition process, which was used as the samples with the hollow blocked. The removal of the BARC layer is carried out by applying an oxygen (O₂) plasma. Stripping the BARC- photoresist yields a cavity, giving rise to uniformly distributed Au-HNPs at the wafer-scale.

SEM

Following optical measurements, the sample was carefully sectioned using a wire cutter, intersecting the device area. Depending on the inspection needs, the resulting fragments were mounted on a stainless-steel sample carrier in either an upright or flat orientation. These mounted fragments were then transferred to a High-Resolution Scanning Electron Microscope (HR-SEM, Merlin, Zeiss) for detailed examination. This allowed both cross-sectional and top-view inspections to assess the structural features and surface properties of the fabricated nanopillars.

TEM images

A substrate with Au-HNPs was coated with a 20 nm carbon film via sputter deposition and transferred to a high-vacuum chamber, where a ~ 3 μ m platinum layer was deposited using Ga⁺-assisted chemical vapor deposition. A ~ 1 μ m thick, 15 μ m long section was then cut using a 30 kV Ga⁺ ion beam at a 4.8° angle to the square unit cell's axis. Before detaching the sample, a wire was welded to the Pt layer for handling. The sample was transferred to a TEM grid, the wire was milled off, and the sample was thinned to 50 ± 10 nm. The angled cut intersected an Au-HNP every 12 periods, providing a representative cross-section.

Optical characterization. Transmission properties were measured by placing the sample in a rotation stage and illuminating it with p-polarized white light (Thorlabs) using a linear array with two polarizers, one acting as a polarizer and the other as an analyzer. UV-VIS Ocean Optics spectrometer collected the transmitted light through an optical fiber.

Molecule-functionalized sample preparation and single-molecule regime optimization.

After fabrication, the sample was labeled with fluorophores by adding a 40:5:1 mixture of Phosphate Buffered Saline (PBS), sodium bicarbonate solution (7.5 %v, Sigma Aldrich) and photoactivatable Abberior CAGE 635 (biotin conjugate) in Dimethylsulfoxide at 0.6 mg/mL (DMSO, Sigma Aldrich) for 30 minutes. In addition, we added polystyrene fluorescent beads dispersed in PBS (Crimson FluoSpheres 200 nm, ThermoFisher Scientific) at low concentration for use as fiducial markers. The sample was rinsed with PBS between each step. After the final step the sample was rinsed with demineralized water. We recorded a continuous acquisition with both the EMCCD (30 ms exposure time) and the SPADs and optimized the photoactivation power so that: i) the PSFs recorded on

the EMCCD were sparse enough to be localized individually (i.e. separated by more than the diffraction limit, around 250 nm), each PSF corresponding to one single emitter, and ii) each SPAD collects the signal of at most one molecule at each time (i.e. if simultaneous emitted molecules occurs in the area of interest of $10\mu\text{m}$ the PSF should be separated by more than $1\mu\text{m}$, which is the separation of the SPADs center to center. If this condition is violated, the data corresponding to both molecules is neglected). Both criteria could be met with a molecule density lower than 1 molecule per μm^2 , which we achieved in the 3D structure by optimizing the photoactivation laser power. Each molecule was thus interrogated individually from its activation to its photobleaching, and the tuning of the photoactivation power ensured that the average activation rate matched the photobleaching rate to maintain a constant density of emitters while still matching the sparsity criterion. The acquisition over extended times (several hours) further ensured optimal detected molecule density, the HTC sample was embedded in a microchamber to control the water volume during long time acquisition, required for stable photophysics properties of the organic molecules. We also optimized the signal-to-noise ratio (SNR) by filtering out the photoluminescence (PL) emission of the Au nanostructure using an optical filter.

Single-emitter fluorescence lifetime experiments.

The optical setup is presented in Fig. 2a. smFLIM was carried out on an inverted microscope body (X71, Olympus) in a wide-field reflection geometry. The fluorescent molecules were excited through the microscope objective with a super continuum pulsed laser (NKT Photonics) coupled to an acousto-optic tunable filter (SuperK Select, NKT Photonics) transmitting a narrow band around a wavelength of 620 nm, the fluorescence detection was from around 640 nm to 700 nm wavelength range, we used a repetition rate of 39 MHz. The excitation polarization was set parallel to the axis of the hollow conical pillars base. Photoactivation of the molecules was achieved with a continuous wave 405 nm laser diode (Oxxius) coupled into the same excitation path as the NKT laser.

A high numerical aperture (NA) objective is important for the efficient collection of photons; we used an oil objective with 1.49 NA and a 100x magnification. The fluorescence emission of the SMs was collected by the same objective and filtered by an emission filter (BLP01-633R, Semrock). The total collection spectrum ranged from 633 nm to 700 nm approximately. and separated in two paths (using a 50:50 beam splitter), which are then detected by an EMCCD camera (iXon Ultra, Andor) and the SPADs array respectively. The exposure time of the EMCCD camera was set to 30 ms. The SPADs array was connected to a time-correlated single photon counting module (TCSPC)⁶¹. Prior to the measurements, the position of each SPAD detector with respect to the CCD field of view (FOV) was calibrated by scanning a fluorescent bead of 200 nm in the sample plane maximizing the intensity in each SPAD with a microstage.

To achieve single-molecule super-resolved maps, it is vital to avoid sample drift during the measurements with nanometer precision. We used a piezoelectric nanopositioner (PI nano XYZ, Physik Instrumente) with a custom stabilization loop algorithm. More precisely, a secondary beam excitation beam is focused on a fluorescent bead, which is subsequently maintained at the same position in z (using the measured intensity as a metric) and in x,y (using the localized position) by the stabilization algorithm. These metrics were measured on the EMCCD camera, and the fluorescent bead is chosen far

from the FOV corresponding to the SPADs array, thus ensuring that the molecules signal is not affected by the bright fiducial marker.

Single-emitter fluorescence lifetime processing.

The principle of the experiment and smFLIM data correlation is shown in Fig. 2b. The single-photon avalanche diode detected single fluorescence photons, and photon detection events were correlated in time to the laser excitation pulses with high-speed electronics of about 1 ps resolution, which enabled us to further construct fluorescence decay. To find the total spontaneous emission decay rate Γ_t (including the radiative and the nonradiative decays) of each single emitter, we applied pulsed excitation and performed time-correlated single photon counting to obtain the detected signal $S(t) = S \exp\left(\frac{-t}{\tau}\right)$ where $\tau = 1/\Gamma_t$ denotes the excited state lifetime and can be directly read from the recorded data. A pulsed excitation at a low repetition rate was employed to leave the emitter enough time to relax to the ground state before the arrival of the next pulse. The customized TCSPC and SPADs array allowed us to attain an excellent combination of high detection efficiency (>30% at 650 nm) and low timing jitter (<60 ps full width at half-maximum, FWHM)^{60,61}.

By correlating the arrival times of the intensity bursts recorded by the SPADs with the events simultaneously detected by the EMCCD camera, the fluorescence decay rate could be associated with the spatial position of the fluorescent event with a subwavelength spatial resolution.

Single-molecule localization microscopy data analysis.

Localization of single-molecule emission was performed by fitting each point spread function (PSF) with a 2D Gaussian function using the ThunderSTORM⁶² plugin in ImageJ⁶³. The obtained location estimates were further processed using a home-built Matlab script, in which single-molecule detections that appear in multiple consecutive frames were first merged and then associated with the time-resolved data recorded by the TCSPC. Frames in which multiple detections coincide with the FOV of a single SPAD were omitted from further data analysis to prevent the mixing of decay rate information of multiple molecules. The typical localization precision ($\sigma_{xy} \sim 14$ nm) was estimated by the median localization precision of all the events that were detected both on the SPAD and EMCCD.

Decay rate estimates were obtained by fitting the decay rate histogram with a mono-exponential decaying function convoluted with the instrument response function (IRF), allowing a small time-shift between the IRF and the recorded decay rate histogram. A background signal was added to the fitting model to correct for background luminescence and dark counts of the SPAD. This background was measured for each single-molecule event in time periods when it was switched off. Fitting optimization was performed by using a maximum likelihood method⁶⁴, assuming a Poissonian distribution of the counts recorded in each time channel.

From the position and decay rate of each correlated single-molecule event, a decay rate map can be reconstructed. Here we choose to plot a scatter plot where each point is a measured value, normalized to the average decay rate of molecules on the substrate surrounded by water in the absence of the nanostructure ($\Gamma_0 \sim 0.3$ ns⁻¹). More information on the smFLIM measurements can be found in^{40,43,44}.

Data overlap for the supercell representation:

To increase the statistical significance of our analysis, we leveraged the periodicity of the HTC lattice to produce a 'supercell' representation that better conveys the spatial distribution of the localized molecules associated with their decay rates. The process is described in Fig. 3a. First, the super-resolved maps shown in Fig. 2 were post-processed to determine the center of each nanostructure, which was later used to draw a 2D square lattice used to merge all the unitary HTC cells into a single *supercell*. Although the period is known (250 nm) with high precision, the angle as well as the origin of the lattice had to be calculated for each acquisition (Fig. 3a). This allowed us to divide the SMLM data into 250x250 nm square unitary cells, each centered on one HTC. We then recombined all these unitary cells in the square lattice to generate a single supercell containing all the molecules detected and correlated in the array of 8 SPADs. Considering that each SPAD is 1 μm diameter and therefore contains approximately 8 complete hollow nanopillars, this allowed us to have approximately 64 times more molecules in the supercell than in a single pillar, for a better statistical analysis

Numerical Simulations. All simulations in this study were performed using the Radio Frequency (RF) module of COMSOL Multiphysics⁶⁵, which employs the finite element method (FEM) to solve Maxwell's equations in the frequency domain. To replicate the experimental configurations, we modeled periodic square arrays with unitary cell of 250 nm of the hollow gold structures of 240 nm high with a hollow truncated nanocones with bottom and top diameters 140 nm and 90 nm respectively, with an inner top diameter of 70 nm, resulting in a top ring thickness around 10 nm. The permittivity of gold, as provided by Johnson and Christy⁶⁶, was used for the material properties.

Additionally, to simulate the periodic array and the substrate that holds the structure, a refractive index of 1.5 was placed below the nanoparticles and 1.33 surrounding the periodic structure.

Purcell factor and decay rate calculations.

The total decay rate (Γ_t) and radiative decay rate (Γ_r), were computed by modeling an electric point dipole positioned in the positions described in the main text, the dipole was placed along the x,y,z-axis of the configurations, oriented parallel or perpendicular to this axis, and positioned 4 nm from the surface of one of the nanoparticles.

The total decay rate (Γ_t) were derived from the self-interaction Green's function, which calculates the electric field (aligned with the dipole moment) induced by the dipole at its own location. The radiative decay rate (Γ_r) was determined by integrating the Poynting vector over a closed spherical surface surrounding the system at a distance of $\sim 1.6 \mu\text{m}$. For normalization, Γ_t and Γ_r were compared to corresponding values obtained for the dipole in an infinite medium made of water with a refractive index of 1.33.

The full simulation environment for all calculations consisted of a box with side of 2000 nm, surrounded by a 400 nm-thick perfectly matched layer (PML) to absorb outgoing waves. The domain was meshed using tetrahedral elements, with the maximum element size kept below $\lambda/10$, where λ is the wavelength of the excitation. A finer mesh was used specifically for the structures. Additionally, a sphere matching the refractive index of water, with a diameter equal to 6nm surrounded the dipole source to ensure an adequately fine grid near the dipole. The mesh surrounding the dipole was finer than 1 nm. The mesh sizes for all simulations were systematically verified to ensure convergence. High performance computer was needed for these calculations to converge.

Supplementary information

SEM images of extended lattice till photograph of wafer scale 3D hollow plasmonic displaced in a 250 nm square lattice. Finite Element Method calculation of the modes excited as a function of the wavelength and illumination angle. Full lattice of the nano-resolved light-matter interaction maps at oblique illumination before correlation with the SPADs array data. Angle calculation and center of mass of data estimation to overlap all data in a Super cell unit cell from all correlated data in the 8 single photon detectors. Full lattice and correlated lattice of the nano-resolved light-matter interaction maps at normal illumination before and after correlation with the SPADs array data. SEM images of 3D hollow geometry filled with polymer. Full lattice and correlated lattice of the nano-resolved light-matter interaction maps at normal illumination for a sample with the cavity filled with polymer before and after correlation with the SPADs array data. Full lattice and correlated lattice of the nano-resolved light-matter interaction maps at oblique illumination for a sample with the cavity filled with polymer before and after correlation with the SPADs array data. Simulated total and radiative decay rate enhancements for a dipole attached to the outer wall of the HTC. Calculated response of a point source coupled to the HTC for P_y polarization.

Acknowledgements

R.M.C.C. thank Rémi Carminati for his valuable discussions. This work has received financial support from the French Agence Nationale de la Recherche via the LABEX WIFI under ANR-10-LABX-24 and ANR-10 IDEX-0001-02 PSL, the ANR SiMPLiFe project ANR-17-CE09-0006 and the ANR MIPTIME project ANR-22-CE09-0030-02. R. M. C. C. and R. W. B. acknowledges the funding by the Canada Research Chairs program under award 950-231657, the Natural Sciences and Engineering Research Council of Canada under the Alliance Consortia Quantum grant ALLRP 578468 - 22 and Discovery Grant RGPIN/2017-06880. M. Z-H acknowledges funding from the Gipuzkoa Quantum program's 2024 call of the Department of Economic Promotion and Strategic Projects of the Provincial Council of Gipuzkoa through the grant awarded to the QSEIRA project (2024-QUAN-000011-01).

Author contributions

R.M.C.C. conceived the project and established the collaborations with other institutions. R.M.C.C., I.I. and V.K. led its development. D.J. and A.S.A. fabricated the Hollow Conical Pillars. R.M.C.C. performed the smFLIM measurements and the data analysis for lifetime and position correlations with inputs from B.V.D., I.I. and V.K.. R.M.C.C. developed the method for the fluorescence labeling of single emitters on HCP. C.C. developed the data filtering functions as well as the tools for the statistical analysis and data representation of the SMLM results. R.M.C.C. characterized the plasmonic modes in the HCP; performed the optical measurements and carried out the full wave solution numerical simulations. M.Z.H. performed the numerical simulations for the Purcell factor. I.I., V.K. and A.S.A. supervised the project. R.M.C.C. wrote the first draft of manuscript with inputs from all authors. C.C. created the figures with input from R.M.C.C. All authors commented on the manuscript and contributed to the scientific discussion.

Competing interests

The authors declare no competing interests.

Additional information

Correspondence and requests for materials should be addressed to R.M.C.C., I.I. and V. K.

Abbreviations

LDOS, local density of states; SERS; SEM, scanning electron microscopy; HTC, hollow truncated nanocones; TCSPC, time correlation single photon counting; LSPR, local surface plasmon resonance; SMLM, single molecule localization microscopy; SPAD, single photon avalanche diode; EMCCD, electron-multiplying charge-coupled device; PSF, point spread function; IRF, instrument response function; FOV, field of view.

References

- (1) Cao, H., Čižmár, T., Turtaev, S., Tyc, T. & Rotter, S. Controlling light propagation in multimode fibers for imaging, spectroscopy, and beyond, *Advances in Optics and Photonics* **2023**, 15(2), 524-612.
- (2) Kim, J., Aghaeimeibodi, S., Carolan, J., Englund, D. & Waks, E. Hybrid integration methods for on-chip quantum photonics, *Optica* **2020**, 7, 291.
- (3) Uppu, R., Midolo, L., Zhou, X., Carolan, J. & Lodah, P. Quantum-dot-based deterministic photon–emitter interfaces for scalable photonic quantum technology. *Nat. Nanotechnol.* **2021**, 16, 1308–1317.
- (6) Arakawa, Y. & Holmes, M. J. Progress in quantum-dot single photon sources for quantum information technologies: A broad spectrum overview, *Appl. Phys. Rev.* **2020**, 7, 021309.
- (7) Javadi, A., Sollner, I., Arcari, M., Hansen, S., Midolo, L., Mahmoodian, S., Kirsanske, G., Pregolato, T., Lee, E.H., Song, J.D., Stobbe, S. & Lodahl, P. Single- photon non-linear optics with a quantum dot in a waveguide, *Nat. Comm.* **2015**, 6,8655.
- (8) Maring, N., Fyrrillas, A., Pont, M., Ivanov, E., Stepanov, P., Margaria, N., Hease, W., Pishchagin, A., Lemaître, A., Sagnes, I., Huong Au, T., Boissier, S., Bertasi, E., Baert, A. Valdivia, M., Billard, M., Acar, O., Briussel, A., Mezher, R., Wein, S. C., Salavrakos A., Sinnott, P., Fioretto, D. A., Emeriau, P.-E., Belabas, N., Mansfield, S., Senellart, P., Senellart, J. & Somaschi, N. A versatile single-photon-based quantum computing platform. *Nat. Photon.* **2024**, 18, 603–609.
- (9) Toninelli, C., Gerhardt, I., Clark, A. S, Reserbat-Plantey, A., Götzinger, S., Ristanović, Z., Colautti, M., Lombardi, P., Major, K. D., Deperasińska, I., Pernice, W. H., Koppens, F. H. L., Kozankiewicz, B., Gourdon, A., Sandoghdar, V. & Orri, M. Single organic molecules for photonic quantum Technologies”, *Nature Materials* **2021**, 20, 1615–1628.

- (10) Yu, C.-J., von Kugelgen, S., Laorenza, D. W. & Freedman, D. E. A. Molecular Approach to Quantum Sensing, *ACS Cent. Sci.* **2021**, 7, 712–723
- (11) Kim, L., Choi, H., Trusheim, M. E., Wang, H. & Englund, D. R. Nanophotonic quantum sensing with engineered spin-optic coupling, *Nanophotonics* **2023**, 1-9.
- (12) E. M. Purcell, Spontaneous emission probabilities at radio frequencies *Phys. Rev.* **1946**, 69, 681.
- (13) K. H. Drexhage, *Progress in Optics*, edited by E. Wolf, North Holland, Amsterdam, **1974**, p. 163.
- (14) Barnes, W. L., Horsley, S. A. R. & Vos, W. L. Classical antennas, quantum emitters, and densities of optical states, *J. Opt.* **2020**, 22, 073501.
- (15) Bouchet, D. & Carminati, R. Quantum dipole emitters in structured environments: a scattering approach: tutorial *J. Opt. Soc. Am. A* **2019**, 36, 186-195.
- (16) Greffet, J.-J., Laroche, M. & Marquier, F. Impedance of a Nanoantenna and a Single Quantum Emitter, *PRL* **2010**, 105, 117701.
- (17) Carminati, R., Cazé, A., Cao, D., Peragut, F., Krachmalnicoff, V., Pierrat, R. & De Wilde, Y. Electromagnetic Density of States in Complex Plasmonic Systems. *Surf. Sci. Rep.* **2015**, 70 (1), 1–41.
- (18) Bozhevolnyi, S. I., Martin-Moreno, L., & Garcia-Vidal, F. *Quantum Plasmonics*. Springer (2018).
- (19) Singh, A., de Roque, P. M., Calbris, G., Hugall, J. T. & van Hulst, N. F. Nanoscale Mapping and Control of Antenna-Coupling Strength for Bright Single Photon Sources, *Nano Lett.* **2018**, 18, 2538–2544
- (20) Zapata-Herrera, M., Florez, J., Camacho, A S. & Ramirez H. Y. Quantum Confinement Effects on the Near Field Enhancement in Metallic Nanoparticles, *Plasmonics* **2018**, 13, 1–7.
- (21) Bohren, C. F. & Huffman, D. R. *Absorption and Scattering of Light by Small Particles*; John Wiley & Sons: New York, **2008**.
- (22) Novotny, L. & Van Hulst, N. Antennas for Light. *Nat. Photonics* **2011**, 5 (2), 83–90.
- (23) Duan, H., Fernández-Domínguez, A. I., Bosman, M., Maier, S. A. & Yang, J. K. W. Nanoplasmonics: Classical down to the Nanometer Scale. *Nano Lett.* **2012**, 12 ,3, 1683–1689.
- (24) Archambault, A., Marquier, F., Greffet, J. & Arnold, C. Quantum theory of spontaneous and stimulated emission of surface plasmons. *Physical Review B* **2010**, 82,3.
- (25) Giannini, V., Fernández-Domínguez, A. I., Heck, S. C. & Maier, S. A. Plasmonic Nanoantennas: Fundamentals and Their Use in Controlling the Radiative Properties of Nanoemitters. *Chem. Rev.* **2011**, 111 (6), 3888–3912.

- (26) Baumberg, J. J., Aizpurua, J., Mikkelsen, M. H. & Smith, D. R. Extreme Nanophotonics from Ultrathin Metallic Gaps. *Nat. Mater.* **2019**, 18 (7), 668-678.
- (27) Muskens, O. L., Giannini, V., Sánchez-Gil, J. A. & Gómez Rivas, J. Strong Enhancement of the Radiative Decay Rate of Emitters by Single Plasmonic Nanoantennas. *Nano Lett.* **2007**, 7 (9), 2871–2875.
- (28) Matsuzaki, K., Vassant, S., Liu, H. W., Dutschke, A., Hoffmann, B., Chen, X., Christiansen, S., Buck, M. R., Hollingsworth, J. A. & Götzinger, S. Strong Plasmonic Enhancement of Biexciton Emission: Controlled Coupling of a Single Quantum Dot to a Gold Nanocone Antenna. *Sci. Rep.* **2017**, 7 (January), 1–11.
- (29) Kühn, S., Håkanson, U., Rogobete, L. & Sandoghdar, V. Enhancement of Single-Molecule Fluorescence Using a Gold Nanoparticle as an Optical Nanoantenna. *Phys. Rev. Lett.* **2006**, 97 (1), 1–4.
- (30) Matsuzaki, K., Liu, H. W., Götzinger, S. & Sandoghdar, V. On Quantum Efficiency Measurements and Plasmonic Antennas. *ACS Photonics* **2021**, 8 (6), 1508–1521.
- (31) Koenderink, A. F. Single-Photon Nanoantennas. *ACS Photonics* **2017**, 4 (4), 710–722.
- (32) Khurgin, J. B. How to Deal with the Loss in Plasmonics and Metamaterials. *Nat. Nanotechnol.* **2015**, 10 (1), 2–6.
- (33) Anger, P., Bharadwaj, P. & Novotny, L. Enhancement and Quenching of Single-Molecule Fluorescence. *Phys. Rev. Lett.* **2006**, 96 (11), 3–6.
- (34) Cao, D., Cazé, A., Calabrese, M., Pierrat, R., Bardou, N., Collin, S., Carminati, R., Krachmalnicoff, V. & De Wilde, Y. Mapping the Radiative and the Apparent Nonradiative Local Density of States in the near Field of a Metallic Nanoantenna. *ACS Photonics* **2015**, 2 (2), 189–193.
- (35) Faez, S., Türschmann, P., Haakh, H. R., Götzinger, S. & Sandoghdar, V. Coherent interaction of light and single molecules in a dielectric nanoguide. *Phys. Rev. Lett.* **2014** 113, 213601.
- (36) Rattenbacher, D. et al. Coherent coupling of single molecules to on-chip ring resonators. *New J. Phys.* **2019**, 21, 062002.
- (37) Mollow, B. R. Stimulated emission and absorption near resonance for driven systems. *Phys. Rev. A* **1972**, 5, 2217–2222.
- (38) Duan, L.-M. & Kimble, H. J. Scalable photonic quantum computation through cavity-assisted interactions. *Phys. Rev. Lett.* **2004**, 92, 127902.
- (39) Caruge, J. M. & Orrit, M. Probing local currents in semiconductors with single molecules. *Phys. Rev. B* **2001**, 64, 205202.
- (40) Córdova-Castro, R. M., van Dam, B., Lauri, A., Maier, S. A., Sapienza, R., De Wilde, Y., Izeddin, I. & Krachmalnicoff, V. Single-emitter super-resolved imaging of radiative decay

rate enhancement in dielectric gap nanoantennas. *Light: Science and Applications* **2024**, 13,7.7

- (41) Jonker, D., Jafari, Z., Winczewski, J.P., Eyovge, C., Berenschot, J.W., Tas, N.R., Gardeniers, J.G.E., De Leon, I. & Susarrey-Arce, A. A wafer-scale fabrication method for three-dimensional plasmonic hollow nanopillars. *Nanoscale advances* **2021**, 3(17), 4926-4939.
- (42) Koenderink, A. F., Tsukanov, R., Enderlein, J., Izeddin, I. & Krachmalnicoff, V. Super-Resolution Imaging: When Biophysics Meets, *Nanophotonics* **2022**, 11(2), 169-202.
- (43) Bouchet, D., Scholler, J., Blanquer, G., De Wilde, Y., Izeddin, I. & Krachmalnicoff, V. Probing Near-Field Light–Matter Interactions with Single-Molecule Lifetime Imaging. *Optica* **2019**, 6 (2), 135.
- (44) Blanquer, G., Van Dam, B., Gulinatti, A., Acconcia, G., De Wilde, Y., Izeddin, I. & Krachmalnicoff, V. Relocating Single Molecules in Super-Resolved Fluorescence Lifetime Images near a Plasmonic Nanostructure. *ACS Photonics* **2020**, 7 (2), 393–400.
- (45) Hess, S. T., Girirajan, T. P. K. & Mason, M. D. Ultra-High Resolution Imaging by Fluorescence Photoactivation Localization Microscopy. *Biophys. J.* **2006**, 91 (11), 4258–4272.
- (46) Rust, M. J., Bates, M. & Zhuang, X. Sub-Diffraction-Limit Imaging by Stochastic Optical Reconstruction Microscopy (STORM). *Nat. Methods* **2006**, 3 (10), 793–795.
- (47) Kim, M. & Rho, J. Metamaterials and Imaging. *Nano Converg.* **2015**, 2 (1), 1-16.
- (48) Córdova-Castro, R. M., Casavola, M., van Schilfgaarde, M., Krasavin, A. V., Green, M., Richards, D. & Zayats, A. V. Anisotropic plasmonic CuS nanocrystals as a natural electronic material with hyperbolic optical dispersion. *ACS Nano* **2019**, 13 (6), 6550-6560.
- (49) Kim, Hongyoon, et al. Optical Metasurfaces for Biomedical Imaging and Sensing. *ACS nano* **2025**.
- (50) Neira, Andres D., et al. Eliminating material constraints for nonlinearity with plasmonic metamaterials. *Nature communications* **2015**, 6 (1), 7757.
- (51) Li, Fajun, et al. Exploring near-field sensing efficiency of complementary plasmonic metasurfaces for immunodetection of tumor markers. *Biosensors and Bioelectronics* **2022**, 203, 114038.
- (52) Nasir, M. E., Krasavin, A. V., Córdova-Castro, R. M., McPolin, C. P. T., Bouillard, J. S. G., Wang, P. & Zayats, A. V. Mode Engineering in Large Arrays of Coupled Plasmonic–Dielectric Nanoantennas. *Adv. Opt. Mater.* **2021**, 9 (11), 2001467.
- (53) Córdova-Castro, R. M., Krasavin, A. V., Nasir, M. E., Zayats, A. V. & Dickson, W. Nanocone-Based Plasmonic Metamaterials. *Nanotechnology* **2019**, 30, 055301.
- (54) Stefaniuk, T., Nicholls, L., Córdova-Castro, R. M., Nasir, M. & Zayats, A. V. Nonlocality-enabled pulse management in epsilon-near-zero metamaterials. *Advanced Materials*,

2022, 2107023.

- (55) Nicholls, L. H., Rodriguez-Fortuno, F. J., Nasir, M. E., Córdova-Castro, R. M., Olivier, N., Wurtz, G. A. & Zayats, A. V. Ultrafast synthesis and switching of light polarization in nonlinear anisotropic metamaterial. *Nature Photonics* **2017**, 11, 628-633.
- (55) Hongtao, W. & Yang, J. K. W. Coevolution of nanophotonics and nanofabrication: achievements and beyond. *Photonics Insights* **2024**, 3 (4), C07-C07.
- (56) Liu, Haotuo, et al. Optical properties of hollow plasmonic nanopillars for efficient solar photothermal conversion. *Renewable Energy* **2023**, 208, 251-262.
- (57) Halas, Naomi. Playing with plasmons: tuning the optical resonant properties of metallic nanoshells. *Mrs Bulletin* **2005**, 30 (5), 362-367.
- (58) Streets, A. M. & Huang, Y. Microfluidics for biological measurements with single-molecule resolution. *Curr. Opin. Biotechnol.* **2014**, 25, 69–77.
- (59) Dittrich, P. S. & Manz, A. Single-molecule fluorescence detection in microfluidic channels the Holy Grail in μ TAS? *Anal. Bioanal. Chem.* **2005**, 382 (8), 1771–1782.
- (60) Bouchet, D., Krachmalnicoff, V. & Izeddin, I. Cramér-Rao Analysis of Lifetime Estimations in Time-Resolved Fluorescence Microscopy. *Opt. Express* **2019**, 27 (15), 21239.
- (61) Cuccato, A., Antonioli, S., Crotti, M., Labanca, I., Gulinatti, A., Rech, I. & Ghioni, M. Complete and Compact 32-Channel System for Time-Correlated Single-Photon Counting Measurements. *IEEE Photonics J.* **2013**, 5 (5), 6801514.
- (62) Ovesný, M., Křížek, P., Borkovec, J., Švindrych, Z. & Hagen, G. M. ThunderSTORM: A Comprehensive ImageJ Plug-in for PALM and STORM Data Analysis and Super-Resolution Imaging. *Bioinformatics* **2014**, 30 (16), 2389–2390.
- (63) Schneider, C. A., Rasband, W. S. & Eliceiri, K. W. NIH Image to ImageJ: 25 Years of Image Analysis. *Nat. Methods* **2012**, 9 (7), 671–675.
- (64) Bajzer, Z., Therneau, T. M., Sharp, J. C. & Prendergast, F. G. Maximum Likelihood Method for the Analysis of Time-Resolved Fluorescence Decay Curves. *Eur. Biophys. J.* **1991**, 20, 247–262.
- (65) COMSOL Multiphysics www.comsol.com
- (66) Johnson, P. B. & Christy, R. W. Optical constants of the noble metals *Phys. Rev. B* **1972**, 6 4370.

Supplementary

Nano-resolved sensing of 3D electromagnetic fields via single emitters' extreme variation of enhanced spontaneous emission

R. Margoth Córdoba-Castro,^{1, 2 *} Dirk Jonker,^{3,4 †} Clement Cabriel,^{1 †} Mario Zapata-Herrera,⁵ Bart van Dam,¹ Yannick De Wilde,¹ Robert W. Boyd,^{2, 6} Arturo Susarrey-Arce,^{3,4} Ignacio Izeddin^{1 *} and Valentina Krachmalnicoff^{1 *}

¹ Institut Langevin, ESPCI Paris, Université PSL, CNRS, 75005 Paris, France.

² Department of Physics, University of Ottawa, Ottawa, ON, Canada.

³ Department of Chemical Engineering, MESA+ Institute, University of Twente, P. O. Box 217, Enschede 7500AE, The Netherlands

⁴ Mesoscale Chemical Systems, MESA+ Institute, University of Twente, Enschede 7500AE, The Netherlands.

⁵ Donostia International Physics Center (DIPC), Paseo Manuel de Lardizabal 4, 20018 San Sebastian, Spain

⁶ University of Rochester, Institute of Optics, Rochester, NY, USA.

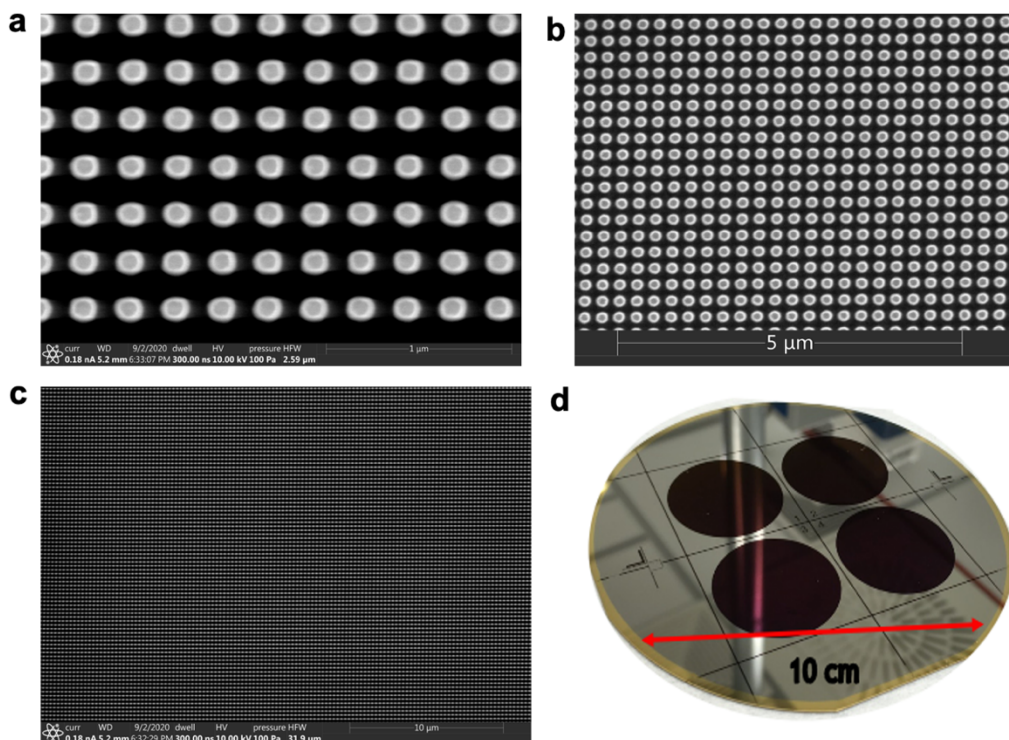


Figure S1: Wafer scale 3D hollow plasmonic displaced in a 250 nm square lattice. Top view Scanning electron microscopy for the Au 3D hollow truncated cones showing the uniform extend of the samples with perfect reproducibility across the wafer scale sample.

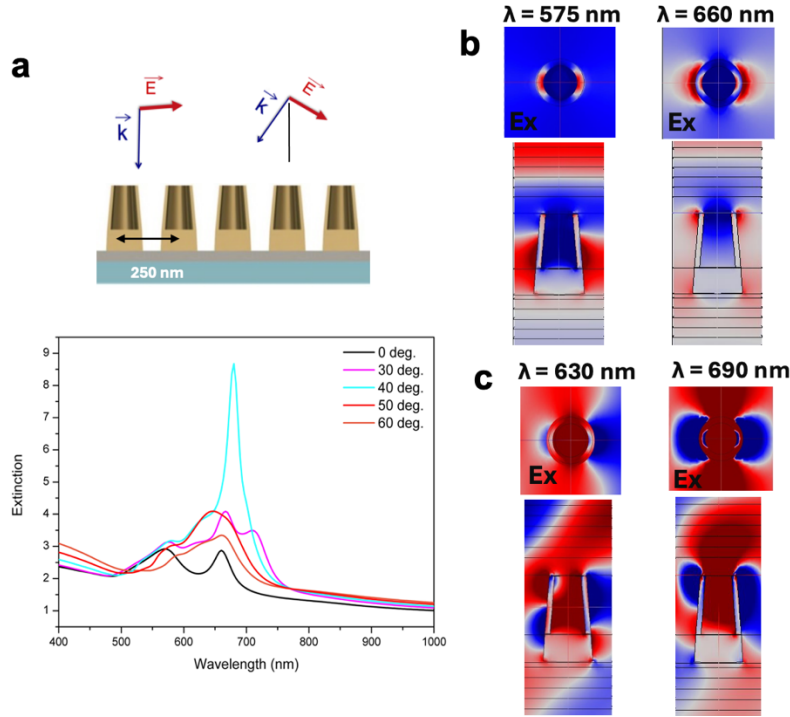


Figure S2: Finite Element Method calculation of the modes excited as a function of the wavelength and illumination angle. (a) Top: illustration of the geometries corresponding to a normal (left) and an oblique (right) illuminations. Bottom: simulation of the extinction spectrum as a function of the illumination angle. (b-c) Normalized simulated near-field electric field maps at different wavelengths for normal (b) and oblique (c) illuminations. The electric field maps are displayed in top view (top) and side view (bottom). These results highlight the diversity of modes that can be excited depending on the illumination conditions.

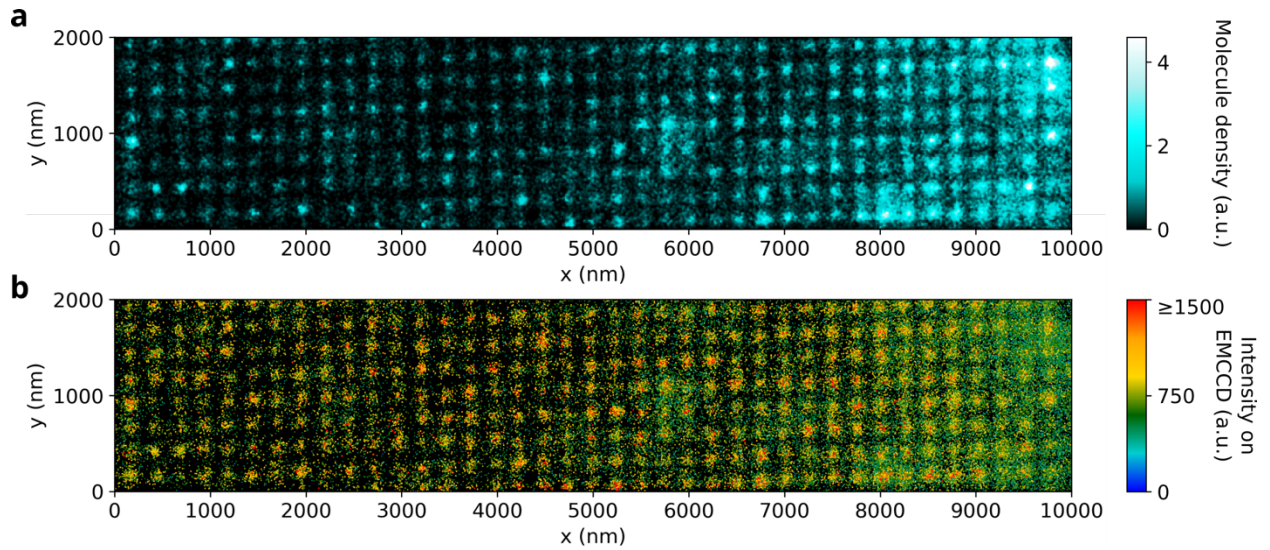


Figure S3: Full lattice of the nano-resolved light-matter interaction maps at oblique illumination before correlation with the SPADs array data. a) Super-resolved map of the density of detected single emitters in an area of $2 \mu\text{m} \times 10 \mu\text{m}$ for an oblique p-

polarized pulsed laser illumination at 620 nm. The density of molecules is represented as a pixelized map. (b) Super-resolved map of the molecule per molecule collected fluorescence intensity in the EMCCD, represented as a scatter plot. Each point represents one detected molecule, and the color encodes its fluorescence intensity.

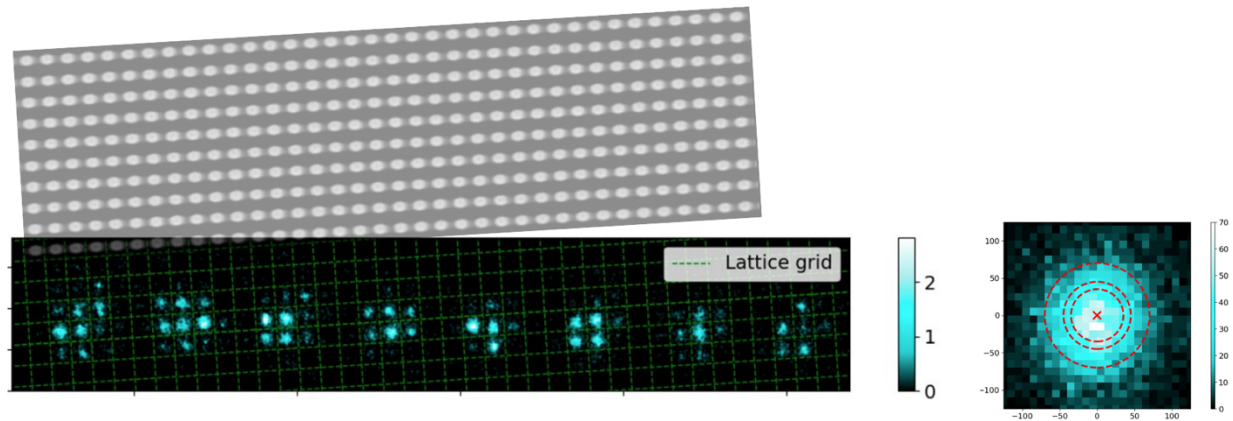


Figure S4: Example of angle calculation and center of mass of data estimation to overlap all data in a Super cell unit cell from all correlated data in the 8 single photon detectors.

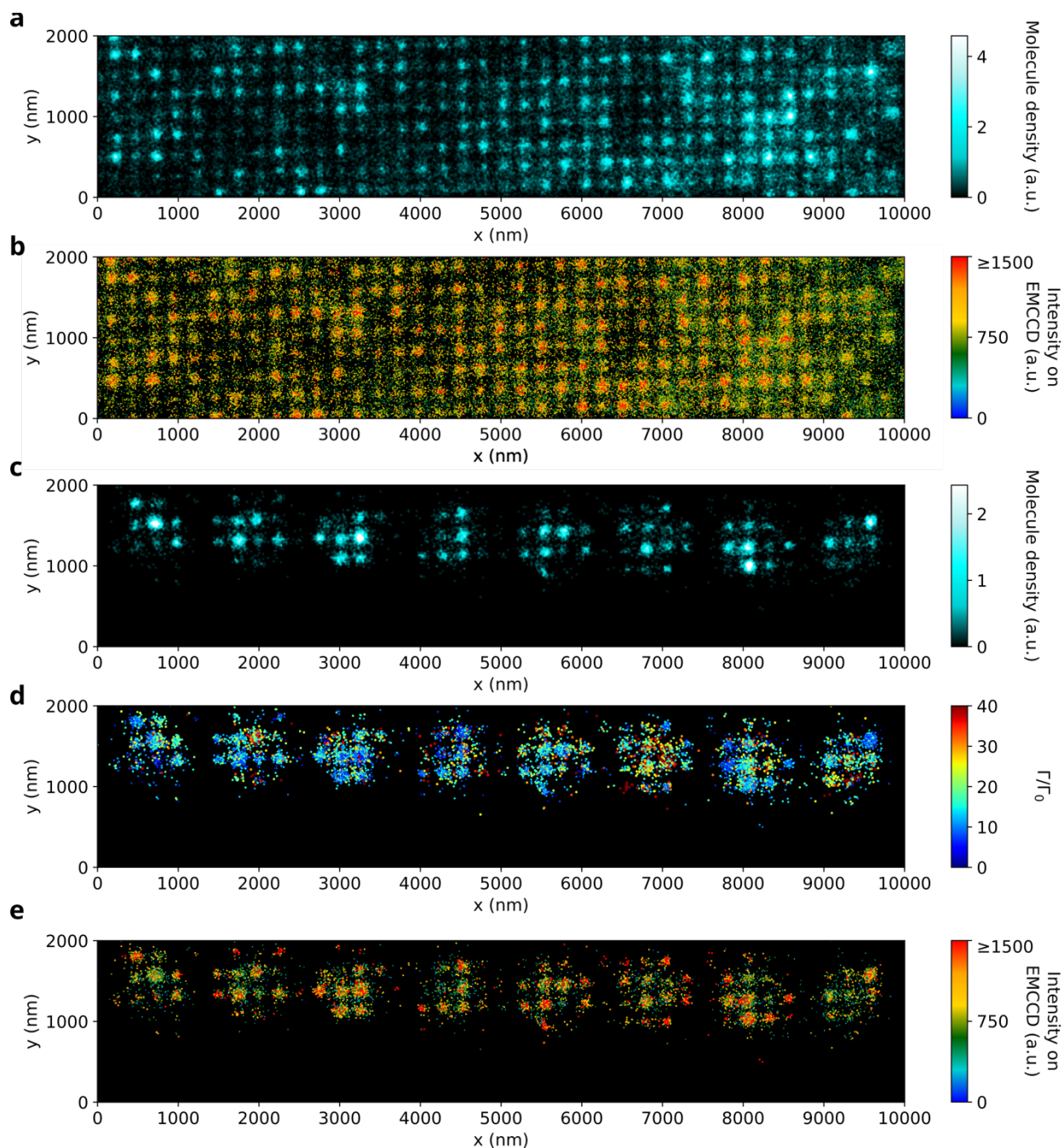


Figure S5: Full lattice and correlated lattice of the nano-resolved light-matter interaction maps at normal illumination before and after correlation with the SPADs array data. a) Super-resolved map of the density of detected single emitters in an area of $2\ \mu\text{m} \times 10\ \mu\text{m}$ for a normal p-polarized pulsed laser illumination at 620 nm before correlation (full lattice). The density of molecules is represented as a pixelized map. (b) Super-resolved map of the molecule per molecule collected fluorescence intensity in the EMCCD, represented as a scatter plot. Each point represents one detected molecule, and the color encodes its fluorescence intensity. (c) Super-resolved map of the density of detected single emitters in the same area and under the same illumination conditions after correlation with the SPADs data (correlated lattice). The density of molecules is

represented as a pixelized map. (d-e) Super-resolved map of the molecule per molecule collected fluorescence intensity in the EMCCD (d) and the decay rate enhancement (e), represented as scatter plots, after correlation with the SPADs data (correlated lattices). Each point represents one detected molecule, and the color encodes its fluorescence intensity or decay rate enhancement.

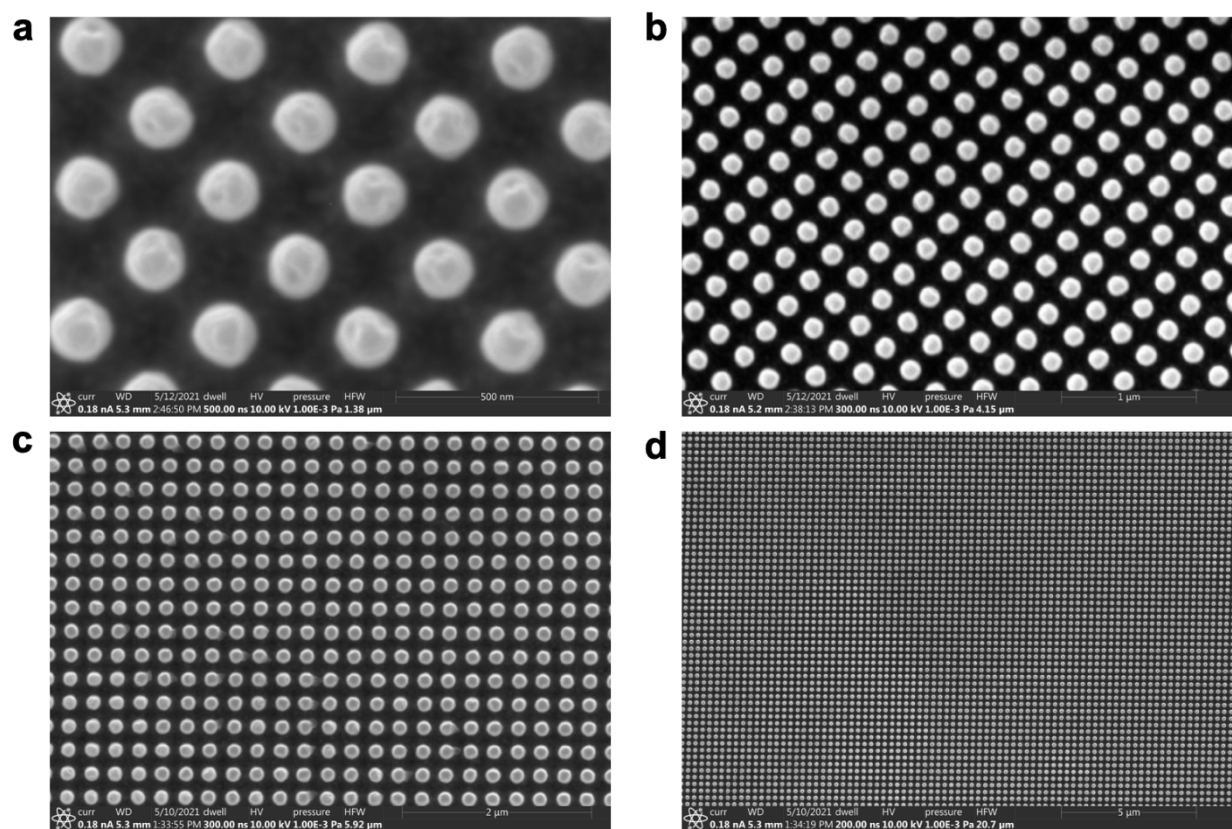


Figure S6: 3D hollow geometry filled with polymer. Top view Scanning electron microscopy of the Hollow Au truncated cones when filled the cavity with a polymer. A) shows the cover of the full cavity with the polymer. b,c) The extended areas shows that the sample only present the polymer inside the cavity without extra coating out of the cavity pillars. d) Shows the consistence of the sample in large area.

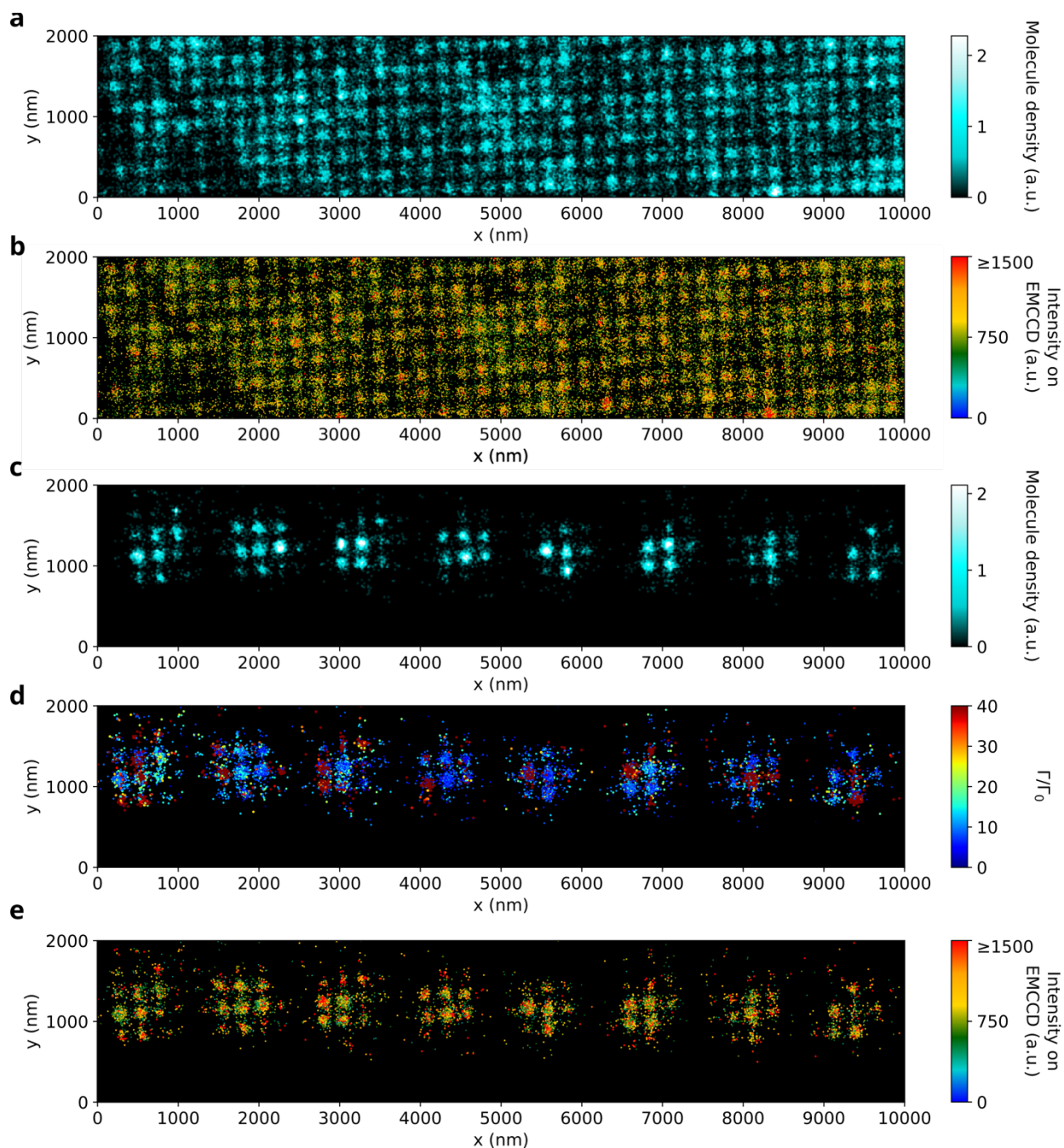


Figure S7: Full lattice and correlated lattice of the nano-resolved light-matter interaction maps at normal illumination for a sample with the cavity filled with polymer before and after correlation with the SPADs array data. a) Super-resolved map of the density of detected single emitters in an area of $2\ \mu\text{m} \times 10\ \mu\text{m}$ for a normal p -polarized pulsed laser illumination at 620 nm before correlation (full lattice). The density of molecules is represented as a pixelized map. (b) Super-resolved map of the molecule per molecule collected fluorescence intensity in the EMCCD, represented as a scatter plot. Each point represents one detected molecule, and the color encodes its fluorescence intensity. (c) Super-resolved map of the density of detected single emitters in the same area and under the same illumination conditions after correlation with the

SPADs data (correlated lattice). The density of molecules is represented as a pixelized map. (d-e) Super-resolved map of the molecule per molecule collected fluorescence intensity in the EMCCD (d) and the decay rate enhancement (e), represented as scatter plots, after correlation with the SPADs data (correlated lattices). Each point represents one detected molecule, and the color encodes its fluorescence intensity or decay rate enhancement.

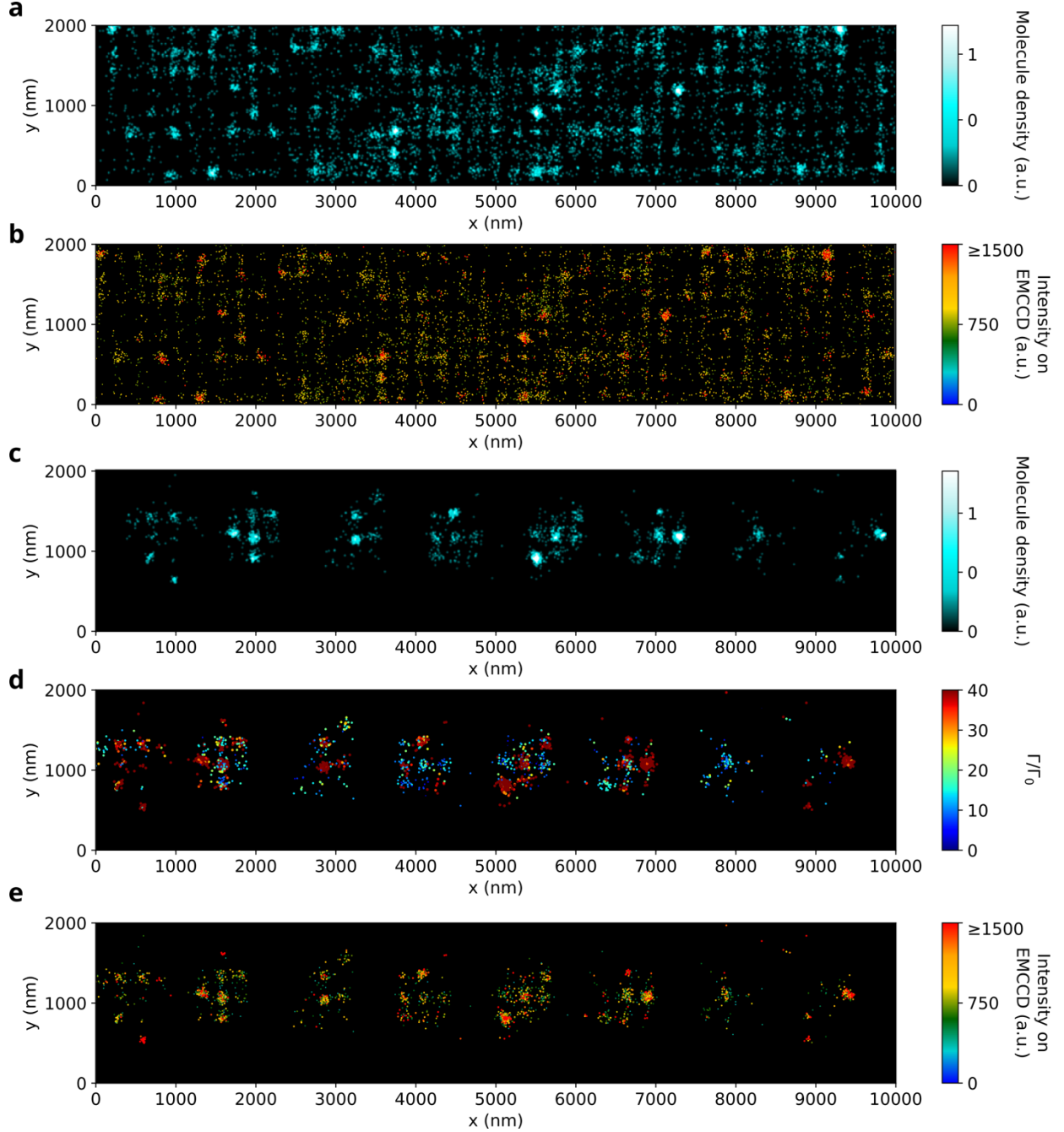


Figure S8: Full lattice and correlated lattice of the nano-resolved light-matter interaction maps at oblique illumination for a sample with the cavity filled with polymer before and after correlation with the SPADs array data. a) Super-resolved

map of the density of detected single emitters in an area of $2\ \mu\text{m} \times 10\ \mu\text{m}$ for a oblique p -polarized pulsed laser illumination at 620 nm before correlation (full lattice). The density of molecules is represented as a pixelized map. (b) Super-resolved map of the molecule per molecule collected fluorescence intensity in the EMCCD, represented as a scatter plot. Each point represents one detected molecule, and the color encodes its fluorescence intensity. c) Super-resolved map of the density of detected single emitters in the same area and under the same illumination conditions after correlation with the SPADs data (correlated lattice). The density of molecules is represented as a pixelized map. (d-e) Super-resolved map of the molecule per molecule collected fluorescence intensity in the EMCCD (d) and the decay rate enhancement (e), represented as scatter plots, after correlation with the SPADs data (correlated lattices). Each point represents one detected molecule, and the color encodes its fluorescence intensity or decay rate enhancement.

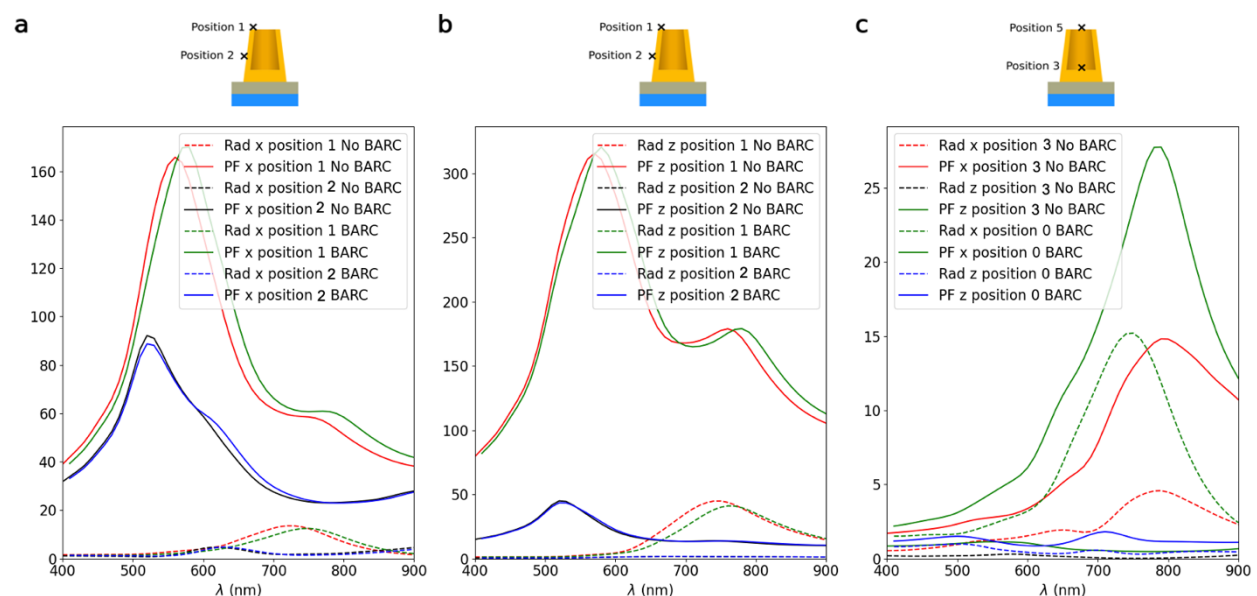


Figure S9: Simulated total and radiative decay rate enhancements for a dipole attached to the outer wall of the HTC (separated by 4 nm) at different positions and with different dipole orientations (see the insets), with and without polymer. Note the different y axes in (a-c). Position 3 is defined only for a non-filled cavity, while position 5 is defined only for a filled cavity. Note that the addition of the polymer changes the decay rate enhancement values only slightly.

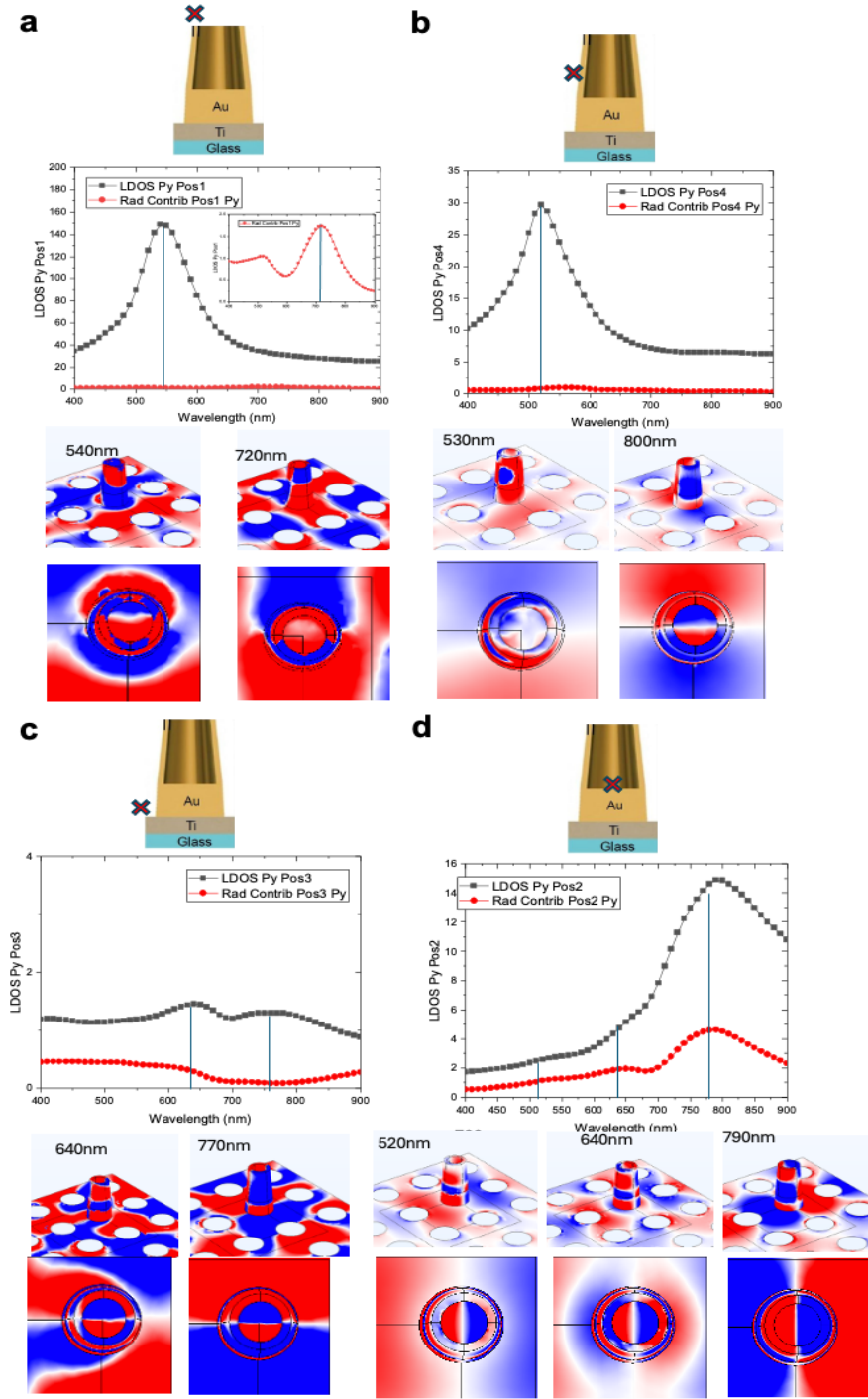


Figure S10: Calculated response of a point source coupled to the HTC for Py polarization. a-d) Simulated total and radiative decay rate enhancements for a dipole attached to the outer wall of the HTC (separated by 4 nm) at different positions (see the insets). The decay rate calculated on the top ring (position 1) is higher than the one sensed by the dipole on the outer wall (position 2) or inside the cavity (position 3). Note the different y axes in (a-d). Also shown in the charge distribution for electric dipoles coupled to the nanosystem at different positions and wavelengths. Each disk represents one HTC.

